Shifting the Paradigm: Redefining the Chronostratigraphy of the Triassic Rewan Group, Bowen Basin, Australia

Matthew Scipione[1], Romain Vaucher[1], Eric Roberts[2], Alex J. McCoy-West[1], Joan Esterle[3], Ashten Turner[1] and Espen Knutsen[1,4]

[1]*Earth and Environmental Sciences, James Cook University, DB34 Discovery Drive, Townsville, Qld 4811, Australia*

[2]*Department of Geology and Geological Engineering, Colorado School of Mines, 1500 Illinois St, Golden, CO 80401, United States*

[3]*School of the Environment, The University of Queensland, Brisbane 4072, Australia*

[4]*Queensland Museum Tropics, Queensland Museum, Townsville, Queensland 4810, Australia*

Correspondence: Matthew Scipione (matt.scipione@my.jcu.edu.au)

Abstract

The Triassic continental Rewan Group in the northern Bowen Basin, Queensland, Australia, consisting of the Sagittarius Sandstone and the Arcadia Formation, preserves a key record of terrestrial environments and faunas that have been assumed to document recovery following the end-Permian mass extinction (EPME). The Rewan Group accumulated in a retroarc foreland basin during the Hunter–Bowen Orogeny, but its chronostratigraphy has remained poorly constrained because previous age models relied mainly on limited, geographically restricted biostratigraphy (esp. palynostratigraphy). Here, we couple detailed lithostratigraphic analysis with high-density U–Pb detrital-zircon (DZ) geochronology by LA-ICP-MS (ca. 300 analyses per sandstone), calibrated against latest Permian (ca. 252–251 Ma) tuffs and a detrital apatite U–Pb dataset, to establish a robust chronostratigraphic framework for the Sagittarius Sandstone and Arcadia Formation. We compare several maximum depositional age (MDA) metrics and show that maximum-likelihood ages (MLA) at 10% discordance provide a stratigraphically coherent MDA estimate, with younger single-grain and cluster-based estimators used as internal checks and minimum bounds. Preferential zircon picking further show that targeted grain selection enriches the youngest Triassic populations, strengthening the robustness of the resulting MDA constraints. The resulting MDAs demonstrate that the Rewan Group spans ca. 250–233 Ma (Olenekian to Carnian) and that the base-Rewan contact is strongly time-transgressive. In the Taroom Trough (foredeep), fluvial successions young consistently up section from the latest Permian (based on tuff ages) through Olenekian–Anisian Sagittarius Sandstone into the late Ladinian–earliest Carnian Arcadia Formation (based on sandstone MDAs). In contrast, in the Denison Trough (back-bulge), the latest Permian coal measures are directly overlain by Middle–early Late Triassic Rewan Group deposits, implying a hiatus or condensed interval of at least ca. 12–15 Myr based on MDAs. We show that known Arcadia Formation vertebrate fossil-bearing horizons are late Ladinian (239 Ma) to early Carnian (236 Ma) rather than earliest Triassic, with the younger date also corroborated by a detrital apatite lower-intercept age of ca. 239 Ma. These revised ages show that the Arcadia Formation vertebrate assemblages do not come from the immediate post-EPME interval but from the late Ladinian to early Carnian, across the onset of the Carnian Pluvial Episode. They provide a dated framework for testing Triassic continental ecosystem evolution in the Bowen Basin and in comparable basins globally.

1. Introduction

The end-Permian mass extinction (EPME, ca. 252 Ma) was the most severe biodiversity crisis in Earth's history, eliminating the majority of marine species and devastating terrestrial ecosystems (McElwain and Punyasena, 2007; Bernardi et al., 2018; Retallack, 2021; Chapman et al., 2022). This collapse reshaped ecological structure, terminating Palaeozoic communities and starting recovery in the Triassic. Early Triassic ecosystems were generally characterized by stressed and low-diversity assemblages dominated by opportunistic taxa, and complete reestablishment of ecological complexity required several million years (Sun et al., 2012; McLoughlin et al., 2020; Chu et al., 2021; Mays and McLoughlin, 2022). Global records document the absence of peat-forming mires ("coal gap") and reef systems ("reef gap") for much of the Early Triassic, reflecting the persistence of extreme environmental conditions (Mundil et al., 2004; Retallack et al., 2005; Botha and Smith, 2006; McLoughlin et al., 2020; Retallack, 2021; Chapman et al., 2022). However, recent marine and terrestrial records show that in some region's ecosystems reestablished within a few million years of the extinction (Brayard et al., 2017; Guo et al., 2025; Roberts et al., 2025). Understanding the tempo and nature of this recovery is central to evaluating how Earth systems reorganize after mass extinction events.

The Bowen Basin of eastern Australia provides one of the most complete continental archives of this recovery in the southern hemisphere (Fig. 1A). Unlike many regions where boundary sections are incomplete, the basin preserves a near-continuous succession from the uppermost Permian Bandanna Formation (and its equivalents) into the Lower Triassic Rewan Group, consisting of the Sagittarius Sandstone and the Arcadia Formation (Fielding and Kassan, 1996; Grech, 2001; Nicoll et al., 2015; Smith et al., 2017; Fig. 2). The Permian–Triassic boundary has been described as an abrupt shift from coal-mire dominated facies to oxidized fluvial red beds of the Sagittarius Sandstone, reflecting the collapse of peat-forming vegetation and shift to braided streams (Fielding et al., 1996; Bashari, 2000; Grech, 2001; Michaelsen, 2002). The overlying Arcadia Formation records fluvial–lacustrine deposition under semi-arid conditions. It contains diverse vertebrate fossil assemblages, including temnospondyl amphibians, fishes, and early reptiles, that provide rare insights into Early Triassic continental ecosystems in Gondwana (Warren, 1980, 1981, 1985; Warren and Black, 1985; Damiani and Warren, 1997; Warren and Marsicano, 1998; Northwood, 1999, 2005; Warren et al., 2001, 2011). Together, these units comprise the Rewan Group, a thick (ca. 500 m to 5 km) stratigraphic succession that captures both environmental change and biotic recovery in a high-latitude Gondwanan setting.

Despite its significance, the Rewan Group's chronostratigraphy remains poorly understood. The absence of volcanic tuffs has prevented direct high-precision dating, leaving the Sagittarius Sandstone and Arcadia Formation constrained only by palynostratigraphy (Green et al., 1997; Bet al., 1998; Grech, 2001; Lang et al., 2001). This uncertainty hampers the assessment of depositional duration, the significance of stratigraphic breaks, correlation with coeval successions in Australia and globally, and reconstruction of Triassic foreland-basin development and sediment routing. It remains unclear whether the transition between the Sagittarius Sandstone and Arcadia Formation reflects continuous sedimentation or a major hiatus, and whether vertebrate fossil-bearing horizons in the Arcadia Formation represent rapid post-extinction recovery or diachronous faunal turnover relative to other Gondwanan basins (Michaelsen, 2002; Benton, 2018; Smith et al., 2018; Sobczak et al., 2024). Without tighter temporal control, the Bowen Basin's potential to inform debates on the tempo of biotic recovery and the synchronicity of ecosystem reorganization worldwide remains underexploited.

In this study, we integrate detailed lithostratigraphic analysis with high-density LA–ICP–MS (Laser Ablation Inductively Coupled Plasma Mass Spectrometry) U–Pb detrital zircon geochronology from sandstones of the Sagittarius Sandstone and Arcadia Formation constrained by latest Permian dated tuffs, to establish a revised chronostratigraphic framework for the Rewan Group. We also obtain a detrital apatite U–Pb age from an Arcadia Formation sandstone at Duckworth Creek as an independent minimum-age check on our zircon-based constraints. Our aims are to refine depositional ages and durations of the Rewan units, evaluate the presence and magnitude of unconformities or condensed intervals at major formation boundaries, and reassess the timing of key vertebrate fossil–bearing horizons within a time-transgressive flexural foreland model for the northern Bowen Basin. This framework strengthens intrabasinal correlation, enables more rigorous comparison with other Gondwanan Triassic basins, and contributes to global discussions on post-EPME Triassic ecosystem evolution.

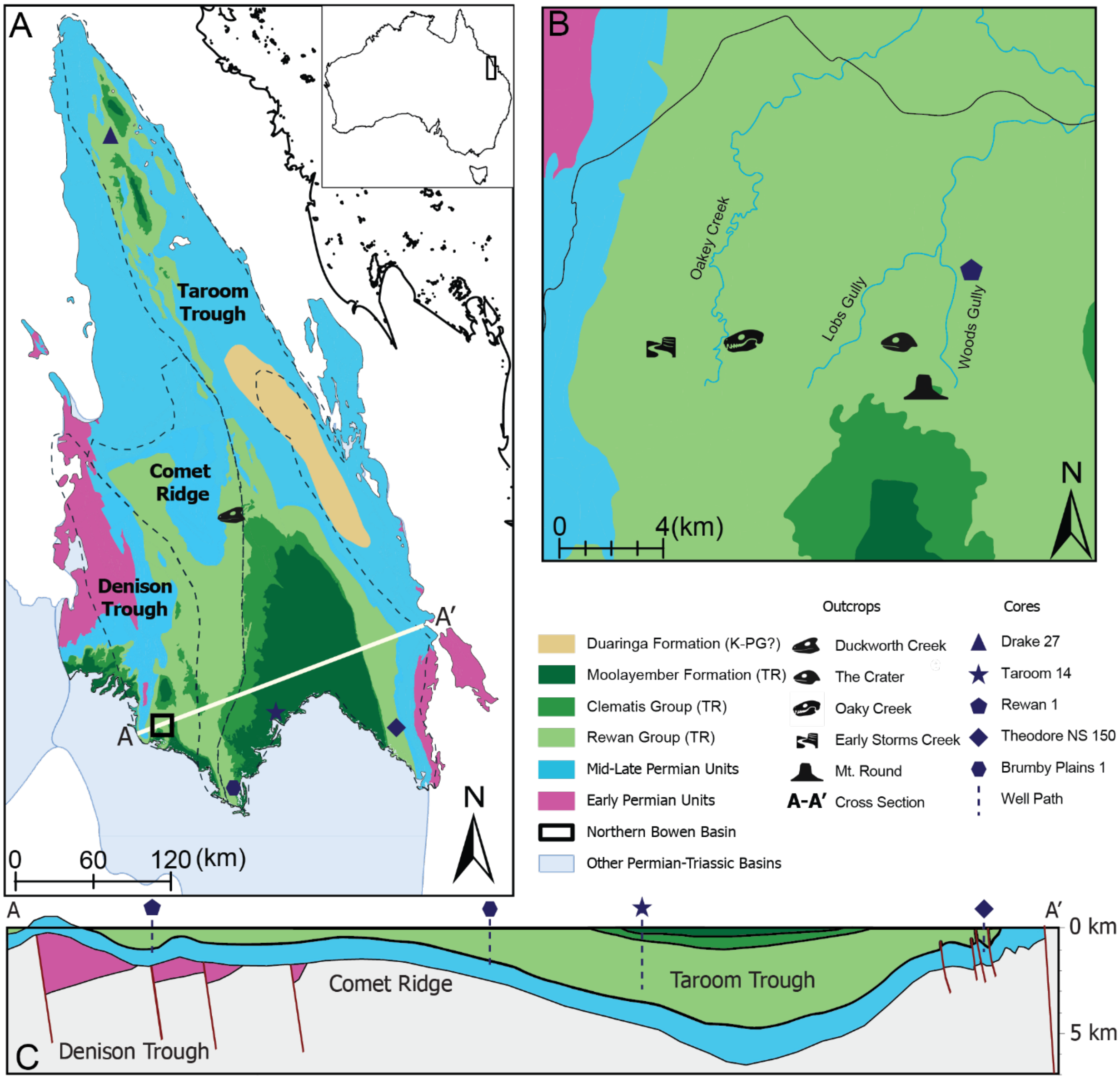

Figure 1. *(A) Map of the northern Bowen Basin, central Queensland, Australia; illustrating Permian units (blue), the Duaringa Formation (tan) and Triassic units (green). Symbols mark zircon sample sites from GSQ stratigraphic cores (red symbols: Drake NS 27, Taroom 14, Rewan 1, Theodore NS 150, Brumby Plains 1) and vertebrate fossil localities at Duckworth Creek, The Crater and Oaky Creek. Major structural elements including the Denison Trough, Comet Ridge and Taroom Trough and Permian–Triassic basin boundaries are overlain. The black outline denotes the extent of the northern Bowen Basin, while the detailed Rewan study area shown in the adjacent panel (Fig. 1B). (B) Enlarged map of the Rewan study area (inset in Fig. 1A), showing Arcadia and Clematis outcrops at The Crater, Oaky Creek, Early Storms Creek and Mount Round, together with the location of the Rewan 1 core. (C) Stratigraphic cross section displaying the three structural regimes as well as projected locations of wells.*

2. Geologic Background

2.1 Tectonic Setting

The Bowen Basin of eastern Australia (Fig. 1) extends over 60,000 km² and contains up to 10 km of Carboniferous to Triassic sedimentary fill (Cadman et al., 1998). During the late Carboniferous, this sedimentary basin occupied high paleolatitudes (ca. 60–80° S) along the Gondwanan margin, where lithospheric extension created a series of half-graben depocentres within the Sydney–Gunnedah–Bowen Basin system (Cadman et al., 1998; Korsch, Totterdell, Fomin, et al., 2009). This early phase of back-arc rifting is widely attributed to slab rollback along the convergent plate boundary (Collins, 1991; Korsch, Totterdell, Cathro, et al., 2009). The resulting sub-basins accumulated thick fluvial and coal-bearing successions, including the Permian coal measures that underlie much of the Bowen Basin (Fielding and Frank, 2014; Kear and Hamilton-Bruce, 2019; Milan et al., 2021; Chapman et al., 2022; Chen et al., 2022; Fielding et al., 2022).

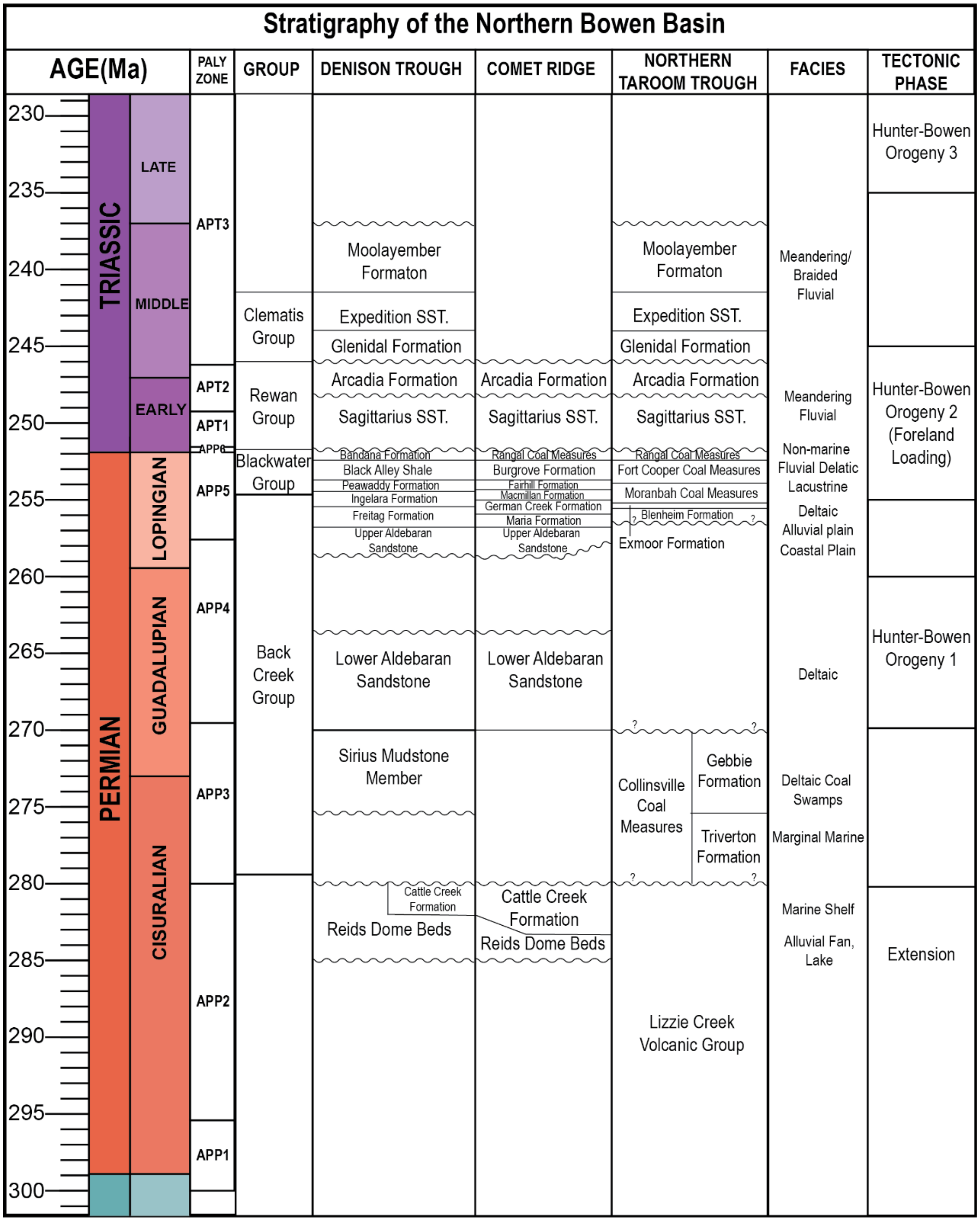

Figure 2. *Stratotectonic chart of the northern Bowen Basin and field localities within the study. The Palynozones are from Smith (2018). The stratigraphic columns are from Jell et al. (2013) and Philips et al. (2017). The tectonic phases after Korsch et al. (2009), Hoy (2020) and Campbell et al. (2022).*

During the early to middle Permian, continued extensional tectonism and subsequent thermal subsidence stabilized the basin, promoting the accumulation of thick, laterally extensive sedimentary successions (Golding et al., 2000; Uysal et al., 2000; Korsch, Totterdell, Cathro, et al., 2009; Fig. 2). This phase laid the structural and stratigraphic foundation for subsequent deformation (Babaahmadi et al., 2021). By the late middle Permian (ca. 270 Ma), convergence along eastern Gondwana had begun, giving rise to the Hunter–Bowen Orogeny (Jessop et al., 2019). Orogenic loading by the advancing New England Orogen produced flexural subsidence in the Bowen Basin, transforming it from an extensional back-arc setting into a retroarc foreland basin (Campbell et al., 2017, 2022; Jessop et al., 2019; Hoy, 2020; Rosenbaum et al., 2020). The initial compressional deformation involved folding, thrusting, and inversion of earlier extensional structures, accompanied by uplift of the eastern hinterland (Korsch et al., 2009; Campbell et al., 2022). This compressive phase drove enhanced foredeep subsidence in the Taroom Trough, forebulge development across Comet Ridge, and back-bulge sag in the Denison Trough (Fig. 1C), shifting the dominant allogenic control on sedimentation from eustatic to tectonic during the late Permian (Fielding et al., 1997; Grech, 2001; Catuneanu, 2004; Campbell et al., 2022).

Foreland basin subsidence persisted into the Early Triassic, punctuated by episodic tectonic events (Phillips et al., 2018). A major deformational pulse at or near the Permian–Triassic boundary produced uplift, erosion of uppermost Permian strata, and a regional unconformity (Korsch et al., 2009; Fig. 2). This deformational event marks the stratigraphic transition from the Permian coal-bearing measures to the Triassic red-bed successions of the Rewan Group. Renewed subsidence in the Early Triassic, possibly linked to continued rollback of the subducting plate, facilitated widespread deposition of the fluvial-lacustrine Sagittarius Sandstone and Arcadia

Formation across the foreland basin (Jensen, 1975; Exon, 1976; Grech, 2001; Brakel et al., 2009). These units record extensive fluvial–lacustrine sedimentation on low-gradient alluvial plains. While the exact duration and intensity of Triassic contraction remain debated, there is a broad consensus that Triassic basin evolution reflects a transition from active orogenesis to thermal relaxation (Jessop et al., 2019; Hoy, 2020; Campbell et al., 2022).

By the Middle Triassic, contractional deformation had diminished, and foreland subsidence transitioned to post-orogenic thermal relaxation, setting the stage for the later development of the overlying Jurassic–Cretaceous Surat Basin. Stratigraphically, this transition is marked by the top of the Rewan Group, overlain by the fluvial sandstones of the Clematis Group and the lacustrine–deltaic Moolayember Formation (Fig. 2), which together signal the onset of a new depositional regime. These relationships are examined in detail in the following section on stratigraphy.

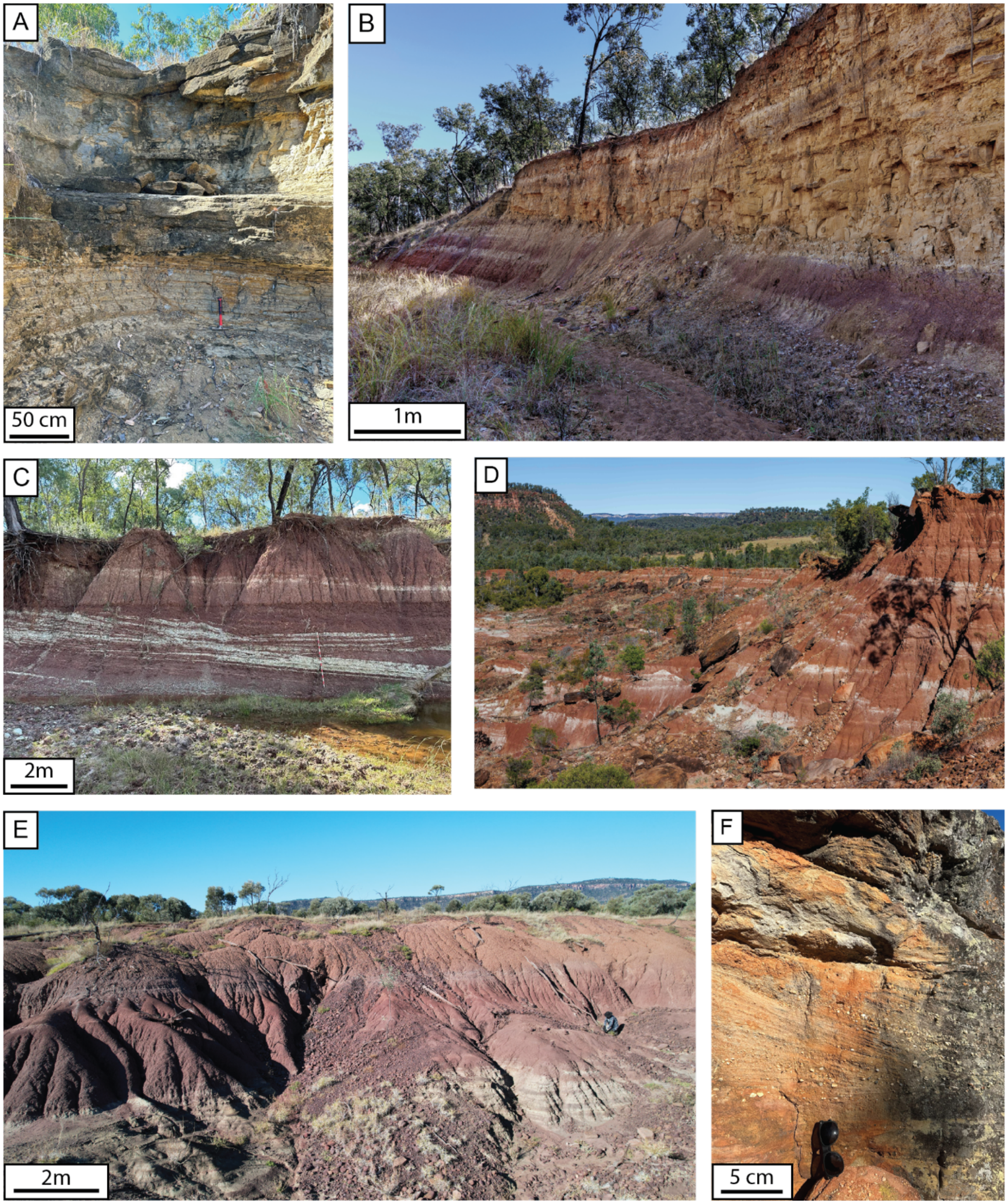

Figure 3. *Outcrop localities and formations for field samples used in detrital-zircon U–Pb geochronology. Panels B to F are sampled sites. (A) Bandanna Formation, reference only with no detrital-zircon sample. (B) Early Storms Creek, Sagittarius Sandstone. (C) Oaky Creek, Arcadia Formation. (D) The Crater, Arcadia Formation, view toward Mount Round. (E) Mount Round, Clematis Group. (F) Duckworth Creek, Arcadia Formation. See Fig. 1 and Table 1 for locations.*

2.2 Stratigraphy

The upper Permian succession of the northern Bowen Basin (Fig. 2) (Blackwater Group) consists of alternating marine mudstones, coal measures, and fluvial sandstones, reflecting repeated transgressive–regressive cycles (Phillips et al., 2017, 2018; Fielding et al., 2022; Naher et al., 2025; Fig. 3, 4A-C). This package is sharply overlain by continental red-bed facies of the Lower Triassic Rewan Group, following the cessation of coal deposition (Jensen, 1975; Fielding and Kassan, 1996; Michaelsen and Henderson, 2000; Lang et al., 2001). In the Taroom Trough, a pronounced erosional disconformity marks the base of the Rewan Group, where it rests directly upon coal measures, whereas in the Denison Trough, the contact is more gradational (Brakel et al., 2009). This basin-wide surface records a relative fall in base level at the Permian–Triassic transition, linked to tectonism and the onset of foreland subsidence.

The Sagittarius Sandstone, forming the basal Rewan Group, represents the initial fluvial influx into the Early Triassic foredeep. It is composed of fine- to medium-grained sandstones with trough cross-bedding, ripple lamination, and scour-and-fill channel bodies, locally capped by wind-rippled bar surfaces that indicate episodic subaerial exposure in semi-arid conditions (Exon, 1976; Green et al., 1997; Grech, 2001; Lang et al., 2001; Fig. 3B, 4D-G). Sandstone channels commonly cut into thick, laterally extensive red siltstone–mudstone floodplain packages (locally the dominant facies), which in outcrop can be difficult to distinguish from the Arcadia Formation red-bed intervals. The base of the Sagittarius Sandstone is widely regarded as a third-order sequence boundary in the sequence-stratigraphic sense, that is, a basin-scale surface produced by a regional fall in base level and associated incision at the Permian–Triassic boundary (Grech, 2001). Compositionally, the Rewan Group succession contains abundant volcanoclastic detritus derived from the New England Orogen, consistent with contemporaneous pulses of silicic arc magmatism (Baker, 1997; Michaelsen and Henderson, 2000; Chapman et al., 2022).

The overlying Arcadia Formation comprises a several-hundred-metre-thick succession of fluvial and overbank deposits that grade upward into red-bed floodplain facies (Fig. 3C-D, 4H). The basal Brumby Sandstone Member records a coarse-grained sandstone, representing a lowstand systems tract(Grech, 2001; Lang et al., 2001). Higher in the succession, interbedded sandstones and mudstones give way to increasingly mud-rich intervals with rooted horizons, mottled paleosols, and calcareous nodules, reflecting more stable floodplain conditions and fluctuating water tables (Jensen, 1975; Exon, 1976; Green et al., 1997; Grech, 2001; Lang et al., 2001; Brakel et al., 2009). An internal sequence boundary is recognized at the base of the Arcadia Formation, marking another phase of incision and renewed channelization. Together, the Sagittarius Sandstone and Arcadia Formation record progressive Early Triassic foreland sedimentation under seasonally arid climatic regimes, with provenance tied to uplifted arc sources along the basin margin (Baker, 1997; Bashari, 2000).

A basin-wide shift in depositional style marks the base of the Clematis Group, where quartz-rich, pebbly sandstones of braided to meandering rivers commonly rest unconformably on the Arcadia Formation (Jensen, 1975; Kassan, 1994; Brakel et al., 2009; Fig. 3E). Increased textural and compositional maturity relative to the volcaniclastic-rich Rewan facies indicates a provenance shift as Hunter–Bowen tectonism waned (Michaelsen and Henderson, 2000; Grech, 2001). Basin-wide synthesis suggests this shift may also record a major reorganisation of dispersal patterns toward greater westerly (cratonic) input, with quartzose sediment reaching even the eastern basin margin (Kassan, 1994). Subsurface correlations on the western side of the basin show the Showgrounds Sandstone as the upper Clematis Group equivalent, locally recording deposition in standing water (lacustrine to shallow-marine), highlighting facies variability across the foreland profile (Green et al., 1997).

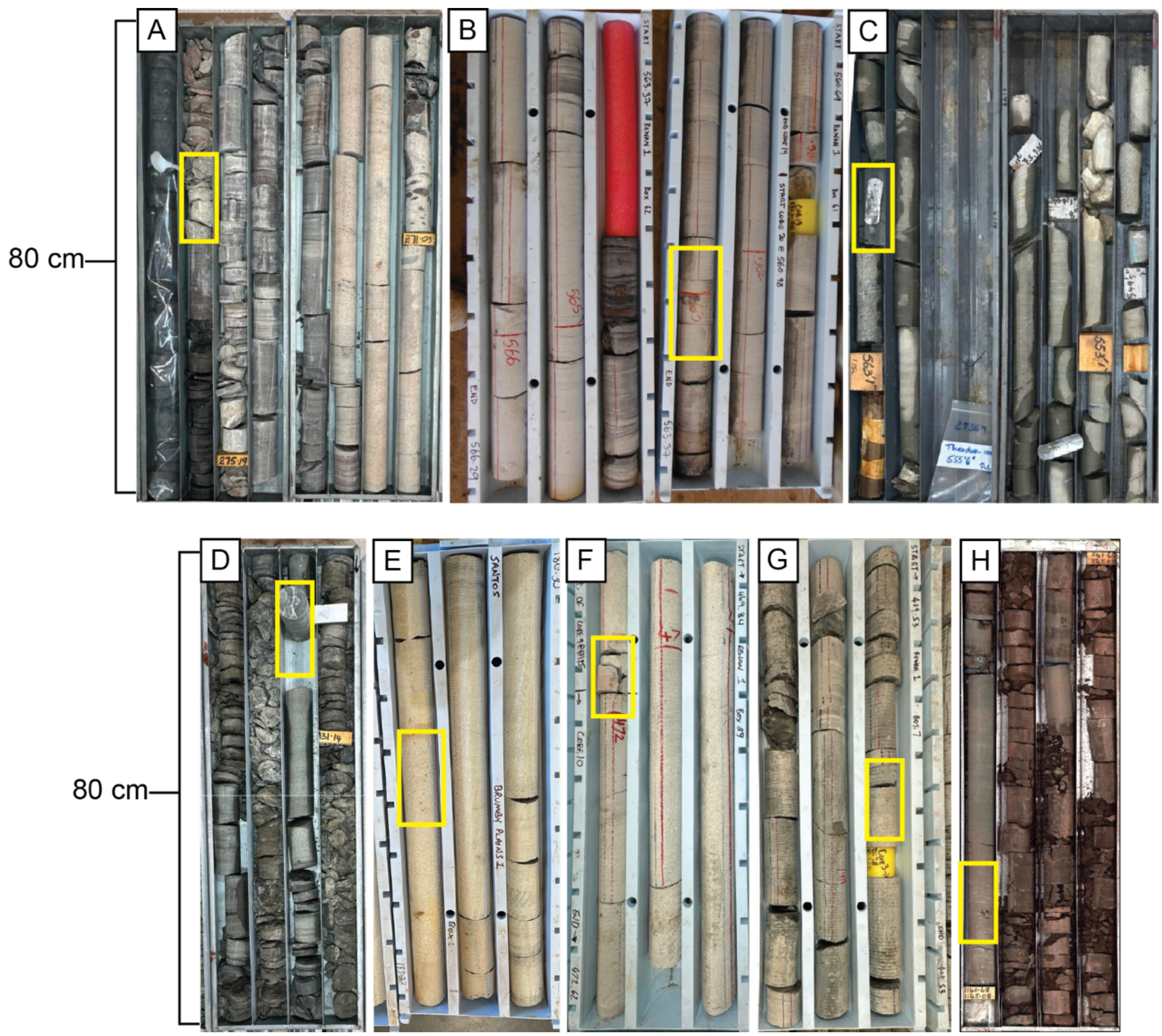

Figure 4. *Core photographs of intervals sampled for U–Pb geochronology across the northern Bowen Basin. Yellow rectangles mark sampled horizons. Scale bars are 80 cm. Panels A to C show volcanic ash beds dated in this study that provide absolute age markers: A, Drake NS27 at 275.6 m, Rangal Coal Measures tuff, Taroom Trough; B, Rewan-1 at 563.1 m, Bandanna Formation tuffaceous mudstone, Denison Trough; C, Theodore NS150 at 171.5 m, tuffaceous debris flow bed immediately above the last coal, Taroom Trough. Panels D to H show detrital sandstones that provide maximum depositional age constraints: D, Drake NS27 at 131.9 m, Sagittarius Sandstone, Taroom Trough; E, Brumby Plains-1 at 183.3 m, Sagittarius Sandstone, Taroom Trough; F, Rewan-1 at 473.5 m, Sagittarius Sandstone, Denison Trough; G, Rewan-1 at 412.1 m, Sagittarius Sandstone, Denison Trough; H, Taroom 14 at 1144.4 m, Arcadia Formation, Taroom Trough.*

The Moolayember Formation (Fig. 2) (Middle–Late Triassic) caps the continental Triassic succession with red–green mudstone and siltstone, subordinate sandstone, and a laterally persistent basal maximum-flooding unit (the Snake Creek Mudstone Member) recorded across the Roma Shelf and adjacent areas (Green et al., 1997; Grech, 2001; Brakel et al., 2009). Regional studies interpret the Snake Creek Mudstone Member as lacustrine to marginal-marine, consistent with a flooding pulse early in Moolayember Formation (Kassan, 1994; Fielding et al., 1996; Green et al., 1997; Michaelsen, 2002). Up-section, the Moolayember Formation coarsens to fluvial sandstones and minor conglomerates before deposition was interrupted by Middle–Late Triassic uplift and erosion, prior to Jurassic subsidence (Green et al., 1997; Lang et al., 2001).

Together, the Rewan Group, Clematis Group, and Moolayember Formation show the Triassic evolution of the Bowen Basin from volcaniclastic-rich foreland infill, to quartzose fluvial systems, and finally to widespread floodplain–lacustrine sedimentation, linking changes in provenance and accommodation to the waning Hunter–Bowen orogen and basin-scale base-level shifts (Exon, 1976; Kassan, 1994; Grech, 2001; Brakel et al., 2009).

3. Methods

3.1 Sampling

Following a comprehensive basin-wide sampling campaign across cores and key outcrops, we selected 13 representative rock samples for detailed zircon U–Pb analysis (Fig. 1): 10 siliciclastic sandstones analysed for detrital zircon maximum depositional ages (MDAs) and 3 Permian tuffs dated as absolute depositional markers. The sampling spans the full stratigraphic range of the Rewan Group from the lower part of the Sagittarius Sandstone to the upper part of the Arcadia Formation, and pairs Triassic detrital targets with underlying Bandanna Formation ash/tuff horizons that anchor the base of Triassic sedimentation. We emphasised volcaniclastic, commonly biotite-bearing sandstones and fossil-adjacent floodplain facies because fresh biotite, volcanic lithic fragments and tuffaceous matrix provide field evidence for direct volcanic input, and such units are therefore the most likely to host juvenile, near-depositional zircon populations that yield robust MDAs (Bashari, 2000; Dickinson and Gehrels, 2009; Barham et al., 2022; Dobbs et al., 2022). For cores we targeted fine- to medium-grained, biotite-bearing volcaniclastic sandstones and tuffaceous mudstones close to key stratigraphic horizons, such as immediately above the last coal seams, within the basal and upper parts of the Rewan Group, and at the base of the Clematis Group. These stratigraphic positions coincide with major facies shifts and increased volcaniclastic influx in the foreland basin and are thus the intervals most likely to record zircons derived from syndepositional ash fall or reworked tuff (Tucker et al., 2013; Dobbs et al., 2022). Core material was examined and sampled at the Geological Survey of Queensland (GSQ) Exploration Data Centre in Zillmere, Brisbane and in archived company repositories. Each sample comprised of 1–5 kg of fresh, unweathered material. Locations, lithologic summaries, coordinates, and depths are listed in Fig. 1 and Table 1.

3.1.1 Lower Rewan Group (Sagittarius Sandstone and basal units)

Outcrops-- At Early Storms Creek (Fig. 1B, 3C) (25.0529° S, 148.3302° E), we sampled the Sagittarius Sandstone as a medium-grained, trough cross-bedded channel sandstone (locally volcaniclastic) from the base of a channel fill, to characterize fluvial channel facies near the base of the Rewan succession.

Cores-- In the Rewan-1 core (Fig. 1B, C; 4B, F, G) (25.0294° S, 148.4311° E), we sampled a Bandanna Formation primary tuff/tuffaceous mudstone at 563.1 m (absolute depositional age anchor, bracketing below the basal Rewan), and within the Sagittarius Sandstone we sampled a biotite-bearing fine-grained sandstone at 412.1 m and a fine–medium sandstone with coal rip-up clasts at 473.5 m (ca. 20 m above the last coal), as detrital targets within the lower part of the Rewan Group channel strata. In the Theodore NS150 core (Fig. 1A, C; 4C) (24.9934° S, 150.0512° E), we sampled a Bandanna Formation primary ash-rich/tuffaceous bed at 171.5 m (absolute depositional age anchor) immediately above the uppermost coal seam at the Permian–Triassic transition (Grech, 2001). In the Drake NS27 core (Fig. 1A, C; 4A) (21.2613° S, 148.0701° E), we sampled a Bandanna Formation primary tuff at 275.6 m (absolute depositional age anchor for the northern basin sector) and a Rewan Group volcaniclastic sandstone at 131.9 m as a mid-succession detrital target. In the Brumby Plains-1 core (Fig. 1A, C; 4E) (25.2814° S, 148.8148° E), we sampled a Sagittarius Sandstone biotite-bearing medium-grained sandstone at 183.3 m, ca. 60 m above the last coal seam along the western Taroom Trough margin.

3.1.2 Upper part of the Rewan Group (Arcadia Formation)

Outcrops— At the location called "The Crater" (Fig. 1B; 3D) (25.0554° S, 148.4094° E), we sampled the Arcadia Formation as a biotite-bearing volcaniclastic sandstone from a crevasse-splay in red-bed floodplain facies at the base to obtain an MDA proximal to the fossil level. At Oaky Creek, Early Storms Station (Fig. 1B; 3C) (25.0587° S, 148.3518° E), we sampled the Arcadia Formation as a biotite-bearing volcaniclastic sandstone from a crevasse-splay. At Duckworth Creek (Fig. 1A; 3F) (23.6162° S, 149.0105° E), we sampled the Arcadia Formation, a volcaniclastic sandstone that overlies an amphibian-bearing bed, indicating floodplain deposition in the northern basin sector. For the upper bounds, at Mount Round (Fig. 1B; 3E) (25.0664° S, 148.4144° E), we sampled the basal part of the Clematis Group as a medium–coarse planar-bedded sandstone to provide an external upper constraint on Rewan deposition.

Cores— In the Taroom 14 core (Fig. 1A, C; 4H) (25.1195° S, 149.1433° E), we sampled the Arcadia Formation as a fine-grained, biotite-bearing sandstone at 1144.4 m, immediately below the Clematis Group, to constrain the upper part of the Rewan Group.

To avoid overstatement, samples are described as commonly biotite-bearing where verified; otherwise, we report facies and grain size consistently and specify mineral indicators only when observed in the hand sample. The three Permian tuffs are non-detrital and were dated as absolute depositional ages; they were not included in detrital MDA calculations. This formation-first organization (older to younger), with explicit coordinates and core depths, and with detrital vs. absolute marker horizons made explicit, provides the stratigraphically constrained framework required for subsequent provenance, depositional timing, and basin evolution analyses.

3.2 Zircon Separation and Imaging

Whole-rock samples were processed for tuff and detrital zircon extraction using a suite of standard mineral-separation techniques at the Mineral Separation Laboratory, James Cook University, Australia. The entirety of each sample was first crushed in a tungsten-carbide mill and sieved to the <500 μm fraction. The sand-sized fraction was then processed through a Wilfley table to remove the clay and most of the light mineral fraction. Samples were then subjected to heavy-liquid separation in lithium metatungstate (specific density ca. 2.87 g/cm³) to isolate the dense mineral phase. Detrital samples were handpicked in two passes (Fig. 5): a random split (ca. 150–200) (Fig. 5B) and a targeted split (ca. 100–150), favouring smaller, blocky, euhedral–subhedral grains with oscillatory zoning (Fig. 5A), to enrich the youngest magmatic component (Coutts et al., 2019; Foley et al., 2021, 2022; Todd et al., 2022). In total, ca. 300 zircon grains were extracted from each siliciclastic sample, and 60–120 grains from each tuffaceous horizon (Fig. 6). Our zircon-picking strategy and dataset-size targets were explicitly informed by the systematic review and numerical experiments of Coutts et al. (2019), who showed that maximum depositional age estimates are most accurate and stable when large numbers of grains are analysed at low analytical uncertainty. In line with those results, we aimed to obtain ~300 zircon analyses per sandstone sample, with 60–120 grains extracted from each tuffaceous horizon. After discordance filtering this typically yielded 150–250 concordant grains per siliciclastic sample, allowing us to treat the resulting ages as conservative MDAs and to test explicitly for hiatuses or unconformities at formation boundaries within the limits of MDA resolution. Selected zircons were mounted in 25 mm epoxy resin pucks, polished to expose mid-sections, and imaged using scanning electron microscopy in both backscattered-electron and cathodoluminescence modes. Scanning Electron Microscopy - Cathodoluminescence (SEM-CL) imaging documented internal zoning, cracks, and inclusions, ensuring that subsequent U–Pb analyses targeted inclusion-free and representative domains within each grain (Tucker et al., 2016, 2017; Foley et al., 2021, 2022; Fig. 5, 6).

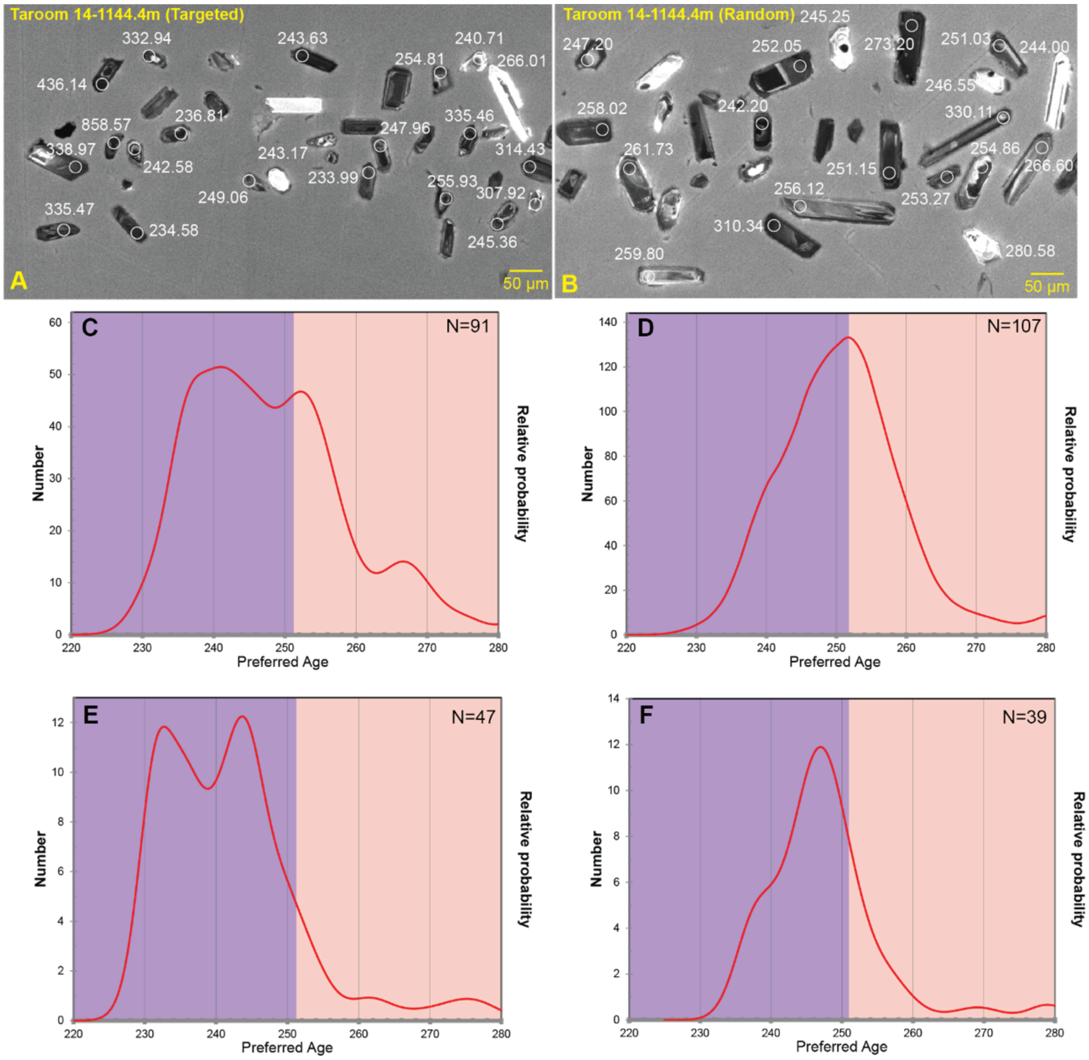

Figure 5. *Zircon-picking experiments comparing targeted versus random grain selection for Triassic sandstones. (A, C) Targeted split from the Arcadia Formation sample Taroom 14 (1144.4 m), showing euhedral–subhedral, short-prismatic grains in SEM-CL (A) and a younger Triassic-peaked KDE for concordant ages between 220–280 Ma (C). (B, D) Random split from Taroom 14, with more variable grain morphologies (B) and a KDE dominated by older, late Permian–earliest Triassic ages (D). (E, F) KDEs for the targeted (E) and random (F) splits of the Sagittarius Sandstone sample in Rewan-1 at 473.3m, again showing enrichment of the youngest Triassic grains in the targeted subset. Scale bars = 50 µm. Background shading indicates Triassic (purple) and Permian (pink)*

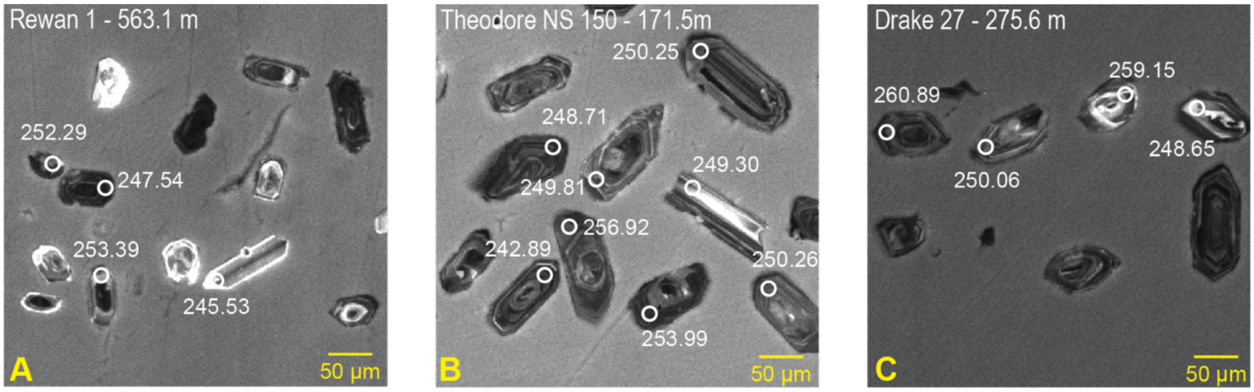

Figure 6. *Cathodoluminescence images of zircon from Permian tuff horizons used as absolute age markers for U–Pb geochronology. Panels A to C show, respectively, A, Rewan 1 at 563.1 m, Bandanna Formation tuffaceous mudstone; B, Theodore NS 150 at 171.5 m, tuffaceous bed immediately above the last coal; C, Drake 27 at 275.6 m, Rangal Coal Measures tuff. Individual spot ages in Ma are annotated next to grains. The scale bar is 50 µm in each panel. These ash beds provide true depositional age that brackets the base of the Triassic succession and anchors the chronostratigraphic framework for the Rewan Group.*

3.3 LA-ICP-MS U–Pb Dating

U–Pb isotopic analyses were performed at the Advanced Analytical Centre, James Cook University, Australia. A 193 nm ArF excimer laser ablation system was coupled to a Laser Ablation Inductively Coupled Plasma Mass Spectrometry (LA-ICP-MS) to conduct *in situ* analyses. Analytical conditions were optimized for accuracy, using a 20 µm spot size and a 10 Hz repetition rate to ablate each grain. This small spot size was chosen to maximize the number of small magmatic zircons analysed. The ablation cell was flushed with He carrier gas, and Ar was added downstream prior to introduction to the plasma. Each analytical session included frequent measurements of zircon reference materials (e.g., GJ-1 and Temora-2 zircon standards) bracketing groups of 10 unknown analyses. A NIST 610 silicate glass standard was analysed periodically to monitor instrument drift and calibrate U and Th concentrations. During analysis, each spot underwent a gas-blank measurement (ca. 30 s with the laser shutter closed, no ablation) followed by ca. 30–45 s of sample ablation. A laser energy density of ca. 5–10 J/cm² and carrier-gas flows was chosen to minimize Pb/U fractionation (by tuning to achieve ca. $^{206}Pb/^{238}U \approx 0.22$ on NIST 610, following standard protocols) (Tucker et al., 2013, 2016, 2017; Todd et al., 2019, 2022; Foley et al., 2020; Cilliers et al., 2021; Henderson et al., 2022).

Raw time-resolved mass spectra were reduced using the Iolite (Paton et al., 2011) software package. The software performed baseline subtraction, downhole fractionation correction, and drift correction using bracketing standards. For each grain, both $^{206}Pb/^{238}U$ and 207Pb/235U dates were obtained. Individual analyses were filtered by concordance: only grains with a 206Pb/238U–207Pb/235U discordance of <10% were retained in detrital samples. A stricter <5% discordance filter was used for the volcanic tuff samples (Dickinson and Gehrels, 2009; Tucker et al., 2017; Coutts et al., 2019; Vermeesch, 2021; Fig. 7). Analyses failing these filters were excluded from age interpretation. Across the dataset, this procedure yielded hundreds of concordant zircon U–Pb analyses per sample (approximately 200 per siliciclastic sample) for MDA analysis.

3.4 Maximum Depositional Age Determination

Multiple MDA metrics were calculated for each zircon dataset using IsoplotR (Vermeesch, 2018) and the Isoplot Excel plugin (Ludwig, 2009). The Youngest Single Grain (YSG) metric represents the age of the single youngest concordant zircon and thus provides a speculative lower bound. In contrast, the Youngest Grain Cluster at 2σ (YGC2σ) is the weighted mean age of the youngest set of at least three concordant grains whose 2σ uncertainties overlap, which effectively excludes any grain whose age does not overlap with that of the coherent youngest population and therefore screens out isolated analytical outliers (Dickinson & Gehrels, 2009). The Youngest Detrital Zircon (YDZ) metric uses Isoplot's Monte Carlo routine to resample a youngest subset of grains (here all analyses within five standard deviations of the single youngest date), repeatedly perturbing their ages within analytical uncertainty and taking the mode of ~10,000 simulated youngest ages as a statistically robust youngest-age estimate with asymmetric uncertainties (Dickinson and Gehrels, 2009; Ludwig K.R., 2009; Tucker et al., 2013; Coutts et al., 2019). The Youngest Statistical Population (YSP) is calculated as the weighted mean age of the youngest subset of more than two grains whose ages form a coherent population with a mean square of weighted deviates (MSWD) near 1, identified by successively adding grains to the youngest pair until the MSWD exceeds 1; the subset with MSWD closest to 1 is taken as the youngest statistical population, and its weighted-mean age and uncertainty are reported as the YSP (Coutts et al., 2019; Herriott et al., 2019). Finally, the Maximum Likelihood Age (MLA) estimator treats the youngest part of the age spectrum as a discrete minimum-age component mixed with an older continuous population and uses maximum likelihood to fit this two-component model to all single-grain ages and their individual analytical uncertainties; the age of the minimum-age component, with its confidence interval, is then taken as the MDA (Vermeesch, 2021). Although YSG yields the youngest possible age and cluster-based metrics such as YGC2σ, YDZ and YSP improve robustness by using multiple grains, MLA makes the fullest use of analytical uncertainties and does not depend on selecting a particular youngest subset. We therefore treat MLA as our primary MDA estimator because it is based on an explicit two component mixture model that uses all single grain ages and their uncertainties, rather than only a handpicked youngest group, and because it behaves as a consistent estimator in numerical tests. Simulation work shows that traditional youngest grain estimators can develop either negative or positive bias as sample size increases, depending on the method and the abundance of near syn-depositional grains, whereas MLA converges on a stable value that closely approximates the true depositional age across a wide range of scenarios (Coutts et al., 2019; Vermeesch, 2021). When MLA is applied to paired LA-ICP-MS and CA-ID-TIMS datasets from the same samples it yields MDAs that agree to within about one percent, while differences between commonly used youngest grain or cluster-based metrics on the same data can reach two to seventeen percent (Vermeesch, 2021). On this basis we adopt MLA derived MDAs as the principal chronostratigraphic constraints for the Rewan Group and report YDZ, YGC2σ and YSP as complementary comparators.

3.5 Apatite Geochronology (corroborative)

To provide an independent minimum-age check on the zircon-based MDA at one key vertebrate fossil horizon, we analysed detrital apatite from a volcaniclastic sandstone of the upper Arcadia Formation at Duckworth Creek (Fig. 1A). Heavy-mineral separates followed the zircon workflow, with hand-picking under a binocular microscope followed by SEM-CL imaging to exclude visibly altered, inclusion-rich, or fractured grains. Forty-nine apatite grains were analysed by LA-ICP-MS on the same instrument configuration described in 3.3, using a 20 µm circular spot, a repetition rate of 5–10 Hz, and identical carrier-gas and plasma conditions. Analytical sessions alternated unknowns with apatite reference materials, MAD and McClure, every five unknowns. MAD is treated as primary and McClure as the secondary U–Pb standards, along with NIST 610 silicate glass to monitor elemental drift and verify downhole fractionation corrections.

Time-resolved signals were reduced in Iolite (Paton et al., 2011) using the VizualAge data-reduction scheme (Petrus and Kamber, 2012; Chew et al., 2014). Because apatite commonly contains significant common Pb and is more susceptible to Pb loss than zircon, ages were calculated on Tera–Wasserburg diagrams with a ^204Pb-based common-Pb correction following Chew et al. (2011) and Xiang et al. (2021) (Fig. 8). We report lower-intercept ages with 2σ uncertainties (Schoene, 2013). We inspected individual analyses in time series space and discarded spots with unstable signals, such as progressive intensity loss, spikes or failure to reach a plateau, before regression. We then filtered on discordance, excluding analyses with greater than 10 percent discordance, and used the remaining population to calculate a single lower intercept age in IsoplotR (Vermeesch, 2018, 2021).

Apatite bearing horizons are sparse in most Rewan Group sandstones, and our aim here was to obtain a corroborative check on depositional timing rather than build a basin wide apatite framework. For that reason, we restricted apatite dating to a single Arcadia Formation sandstone immediately above one of the fossil amphibian bearing beds at Duckworth Creek. We therefore treat the apatite U-Pb result as a corroborative minimum age that is compared directly with the zircon MDA metrics from the same bed, rather than as an independent depositional age for the unit (Finzel et al., 2025).

4. Results

Detrital zircon U–Pb data were obtained from ten Triassic sandstone samples and three underlying Permian tuff or tuffaceous horizons distributed across the Denison Trough, Comet

Sample	Locality	GPS Coordinates (X)	GPS Coordinates (Y)	Formation	No. Analyses	YSG (Youngest Single Grain)	YDZ (10%) (Gehelles)	YGC (±2σ) (10%)	YSP (Coutts et al, 2019)	MLA (%10) (Veermesch, 2021)
CT-23-31	Crater	148.409404°E	25.055433°S	Arcadia Formation	363 analyses; 142 Concordant	231.48 ± 5.55; 3.18% Discordant	229.67 +3.5/-6.5 Ma	236.9 ± 1.2; MSWD .76 ; 22 grains	237.98 ± 2.87 Ma; MSWD=.99; 29 grains	239.0 ± 1.6
ES-23-31	Oakey Creek (Early Storms)	148.351756°E	25.058705°S	Arcadia Formation	334 analyses; 216 Concordant	229.26 ± 10.25; 3.35% Discordant	227.92 +5.3/-10 Ma	236.2 ± 2.1; MSWD 0.82; 13 grains	238.32 ± 2.89 Ma; MSWD=.99; 21 grains	239.2 ± 3.2
ES-23-22	Early Storms Creek	148.330166°E	25.052905°S	Sagitarrius SS	330 analyses; 121 Concordant	233.89 ± 4.68; 2.07% Discordant	234.33 +4.6/ -5.7 Ma	246.4 ± 2.5; MSWD 1.01; 5 grains	246.4 ± 3.83 Ma; MSWD=1.01; 5 grains	237.6 ± 4.7 Ma
DW-24-03	Duckworth Creek	149.010494°E	23.616194°S	Arcadia Formation	301 analyses; 144 Concordant	228.50 ± 6.21; 1.25% Discordant	225.67 +3/-5.5 Ma	233.2 ± 1.3; MSWD 0.77; 24 grains	234.5 ± 3.1 Ma; MSWD= 0.98; 31 grains	235.9 ± 2.0 Ma
CT-24-01	Mount Round	148.4144415°E	25.0664199°S	Clematis Group	320 analyses; 186 Concordant	223.83 ± 6.94; 4.05% Discordant	222.08 +5.6 /-6.2 Ma	229.3 ± 3.8; MSWD 1.7; 7 grains	227.5 ± 3.94 Ma; MSWD=1.15; 5 grains	227.4 ± 6.1 Ma

Sample	Well Name -Depth	GPS Coordinates (X)	GPS Coordinates (Y)	Formation	No. Analyses	YSG (Youngest Single Grain)	YDZ (10%) (Gehelles)	YGC (±2σ) (10%)	YSP (Coutts et al, 2019)	MLA (%10) (Veermesch, 2021)
RW1-24-03	Rewan 1 - 412.1m	148.4310983°E	25.0293992°S	Sagittarius SS	302 analyses; 262 Concordant	230.79 ± 7.30; 7.30% Discordant	229.67 +3.7/-5.7 Ma	236.7 ± 1.3; MSWD 1.14; 14 grains	236.37 ± 2.85 Ma; MSWD=1.03; 13 grains	237.7 ± 2.5 Ma
RW1-24-07	Rewan 1 - 473.5m	148.4310983°E	25.0293992°S	Sagittarius SS	300 analyses; 202 Concordant	230.17 ± 4.77; 4.87% Discordant	227.67 +2.7 -4.4 Ma	234.4 ± 1.2; MSWD 1.3; 27 grains	233.77 ± 2.82 Ma; MSWD=1.00; 22 grains	233.2 ± 2.2 Ma
BP1-24-03	Brumby Plains 1- 183.3m	148.8148042°E	25.2814422°S	Sagittarius SS	300 analyses; 176 Concordant	241.11 ± 6.00; 3.01% Discordant	238.33 +4.4 -5.7 Ma	247.7 ± 1.6; MSWD 0.90; 21 grains	248.0 ± 3.0 Ma; MSWD= 0.98; 22 grains	249.8 ± 2.7 Ma
T14-25-09	Taroom 14 - 1144.4m	149.1432502°E	25.1195134°S	Arcadia Formation	300 analyses; 279 Concordant	230.52 ± 4.32; 2.28% Discordant	228.33 +3.1 -5.7 Ma	234.8 ± 1.2; MSWD 0.64; 18 grains	237.1 ± 3.1 Ma; MSWD= 0.98; 40 grains	237.8 ± 1.6 Ma
D27-25-01	Drake 27 - 131.9m	148.0701224°E	21.2613481°S	Sagittarius SS	300 analyses; 200 Concordant	242.48 ± 5.75; 3.47% Discordant	240.33 +2.8 -5.3 Ma	246.6 ± 1.4; MSWD 0.64; 20 grains	247.1 ± 3.3 Ma; MSWD= 1.07; 21 grains	245.9 ± 1.9 Ma

Sample	Well Name -Depth	GPS Coordinates (X)	GPS Coordinates (Y)	Formation	No. Analyses	YGC(±2σ) 5%	Concordia Age
TNS-25-04	Theodore NS 150-171.5m	150.0512325°E	24.9934372°S	P/T Boundary	167 analyses; 79 Concordant	250.5 ± 0.95; MSWD 1.7; 72 grains	251.8 ± 0.6; MSWD 1.7; 72 grains
RW1-25-03	Rewan 1-563.1m	148.4310983°E	25.0293992°S	Bandanna Formation	100 analyses; 38 Concordant	250.0 ± 1.2; MSWD 1.13; 38 grains	251.4 ± 1.9; MSWD 0.36; 38 grains
D27-25-03	Drake 27-275.6	148.0701224°E	21.2613481°S	Rangal Coal Measures	64 analyses; 22 Concordant	251.7 ± 1.7; MSWD 1.5; 22 grains	252.6 ± 1.2; MSWD 1.5; 22 grains

Table 1. *Summary of U Pb detrital zircon and tuff U Pb results from outcrop and core samples in the northern Bowen Basin. For each sample, the table lists locality, coordinates, formation, number of analyses and concordant grains, and maximum depositional age metrics including youngest single grain (YSG), youngest detrital zircon (YDZ), youngest grain cluster (YGC), youngest statistical population (YSP) and maximum likelihood age (MLA), together with 5 percent discordance YGC and Concordia ages for Permian tuffs.*

Ridge, and northern Taroom Trough (Fig. 1, 3, 4; Table 1). For each sandstone sample, we calculated multiple MDA estimators (YSG, YDZ, YGC2σ, YSP, MLA) using the filtering criteria outlined in Sections 3.3–3.4. Complete analytical results, including per-grain data and all MDA metrics, are compiled in Table 1 and the Supplementary Appendix.

4.1 Permian tuff horizons (Bandanna Formation and Rangal Coal Measures)

The three tuff or tuffaceous beds immediately beneath the Rewan Group yield tightly clustered late Permian U–Pb zircon ages. Concordant populations from the Bandanna Formation tuff in Rewan-1 and the Rangal Coal Measures tuffs in Drake NS27 and Theodore NS150 give weighted-mean and Concordia ages of ca. 252–250 Ma (Changhsingian–earliest Induan; Fig. 7; Table 1). These ages are consistent with published CA–ID–TIMS constraints for correlative marker horizons and provide direct depositional ages for the uppermost coal measures (Ayaz et al., 2016; Metcalfe et al., 2024). They also establish a latest Permian temporal reference surface immediately below the Triassic succession.

Cathodoluminescence images of zircon from these three tuffs (Rewan-1, Theodore NS150, and Drake 27; Fig. 6) show populations dominated by euhedral to subhedral, short-prismatic to elongate grains with well-developed oscillatory zoning and only minor rounding. Zircons from Rewan-1 are generally smaller (Fig. 6A), with long axes of about 70–160 µm, whereas crystals from Theodore NS150 and Drake 27 include a higher proportion of larger grains (Fig. 6B-C), with long axes commonly 90–220 µm and locally up to ~240 µm. Most analysed domains lack pervasive resorption or complex inherited cores, consistent with derivation from single volcanic eruptions and supporting the interpretation of these beds as reliable true depositional age.

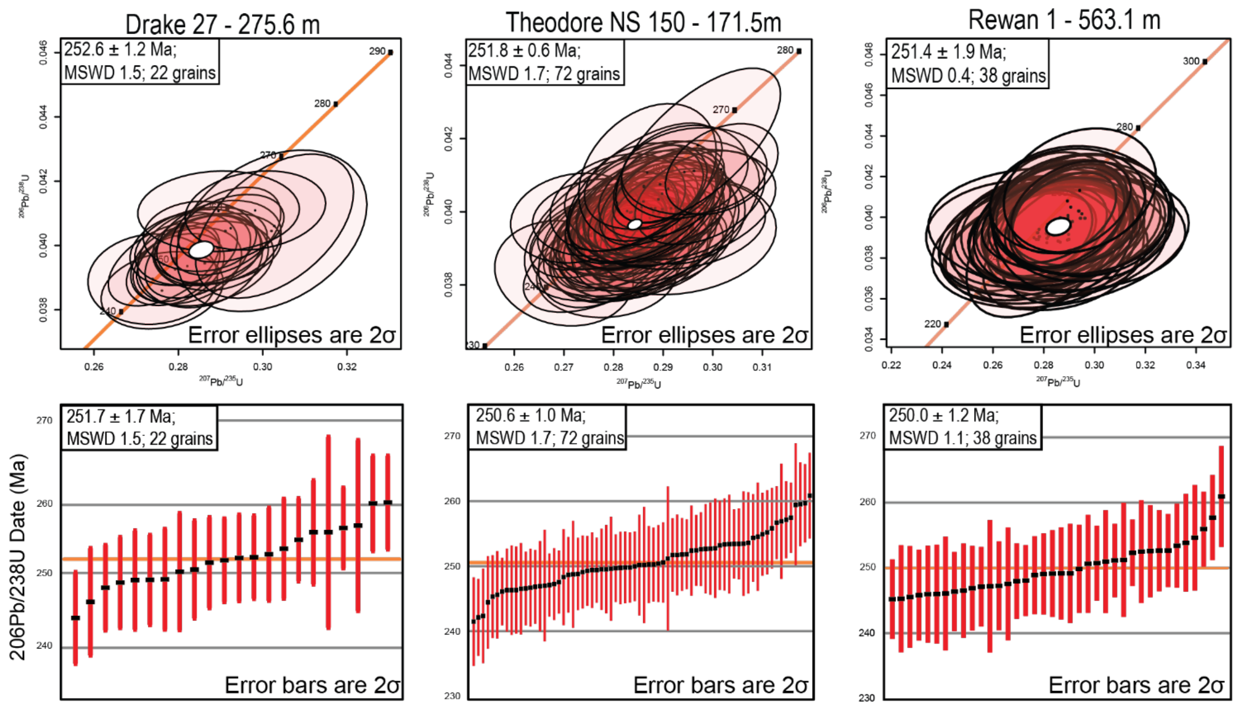

Figure 7. *Concordia and weighted-average age analyses for volcanic tuff samples from three stratigraphic wells in the northern Bowen Basin. Top row: U–Pb Concordia plots for the Drake 27 tuff at 275.6 m (n = 22; 252.6 ± 1.2 Ma; MSWD 1.5), Theodore NS 150 tuff at 171.5 m (n = 72; 251.8 ± 0.6 Ma; MSWD 1.7) and Rewan 1 tuff at 563.1 m (n = 38; 251.4 ± 1.9 Ma; MSWD 0.4). Error ellipses denote 2σ uncertainty. Bottom row: corresponding* $^{206}Pb/^{238}U$ *weighted-average age histograms with 2σ error bars; orange lines mark the weighted-mean age for each sample.*

4.2 Sagittarius Sandstone (Lower part of the Rewan Group)

Sagittarius Sandstone samples are characterised by zircon age spectra dominated by Triassic populations with subordinate late Permian components (Fig. 9; Table 1). Maximum-likelihood MDAs for these samples span the Early to–early Late Triassic. Along the western margin of the Taroom Trough (Brumby Plains-1, Drake NS27), MLA-based MDAs fall in the Olenekian to late Anisian (ca. 250–246 Ma), indicating that these strata were deposited after ca. 250–246 Ma. In contrast, Sagittarius Sandstone samples from the Denison Trough (Rewan-1 core and associated outcrops) yield younger MLA-based MDAs in the Ladinian to earliest Carnian (ca. 238–233 Ma), implying that comparable stratigraphic levels post-date ca. 238–233 Ma.

Across all Sagittarius Sandstone samples, the MDA estimators display a consistent rank order (YSG/YDZ ≤ YGC2σ ≈ YSP ≤ MLA). We therefore adopt the MLA values as the preferred maximum depositional age constraints for stratigraphic comparison and use the younger single-grain estimators as minimum bounds that are not themselves interpreted as depositional ages. All alternative metrics are reported in Table 1 for transparency.

4.3 Arcadia Formation (Upper part of the Rewan Group)

Arcadia Formation sandstones from The Crater, Oaky Creek, Duckworth Creek, and the Taroom 14 core yield concordant Triassic zircon populations, with the youngest coherent components falling within the late Ladinian to early Carnian (ca. 239–236 Ma; Fig. 9, 10; Table 1). MLA-based MDAs for these samples cluster in this interval, indicating that deposition throughout the study area occurred after ca. 239–236 Ma in the Arcadia Formation. Denison Trough outcrop samples (The Crater, Oaky Creek) typically yield late Ladinian MDAs, whereas Comet Ridge and Taroom Trough samples (Duckworth Creek, Taroom 14) produce slightly younger early Carnian MDAs. These MDA results minimally place the vertebrate fossil-bearing horizons at The Crater and Duckworth Creek within the Middle–early Late Triassic rather than in the earliest Triassic, as previously suggested. This temporal revision has direct implications for palynostratigraphic correlation and for interpreting the Arcadia vertebrate record and recovery tempo, which are discussed further in Section 5.4.

Detrital apatite U–Pb data from the Arcadia Formation sandstone at Duckworth Creek yield a Tera–Wasserburg lower-intercept age of 239.3 ± 6.6 Ma (2σ; MSWD = 0.79; n = 49), corresponding to a late Ladinian–early Carnian interval (Fig. 8; Table 1). Within uncertainty, this age is consistent with the zircon-based MLA for the same bed (235.9 ± 2.0 Ma), and we therefore treat the apatite result as a minimum-age constraint that corroborates the zircon-derived timing of deposition rather than as an independent depositional age estimate.

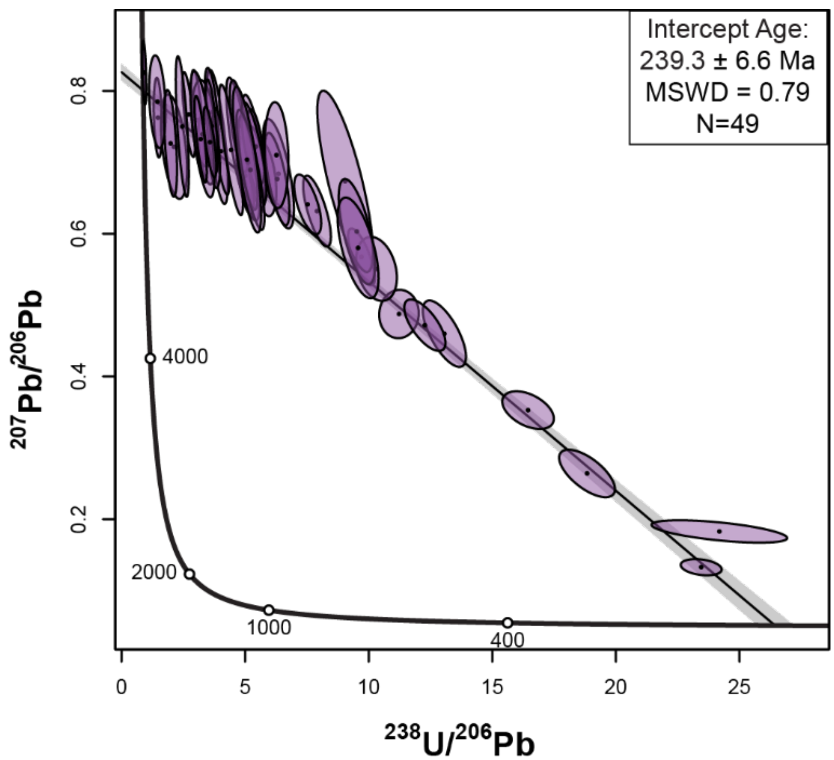

Figure 8. *Detrital apatite U–Pb Tera–Wasserburg Concordia plot for the Arcadia Formation sandstone at Duckworth Creek (Comet Ridge). Regression of 49 analyses yields a lower intercept age of 239.3 ± 6.6 Ma (2σ; MSWD = 0.79); ellipses show 2σ uncertainties. The apatite intercept provides an independent minimum-age constraint that is consistent, within uncertainty, with the zircon MDA metrics from the same bed (MLA = 235.9 ± 2.1 Ma; YGC2σ = 233.2 ± 1.3 Ma), supporting a Carnian MDA at Duckworth Creek (see Table 1; Fig. 4).*

4.4 Clematis Group

The basal part of the Clematis Group sandstone exposed at Mount Round contains a Triassic-dominated detrital zircon population with the youngest coherent component in the Late

Triassic. The MLA-derived MDA lies in the late Carnian (ca. 227 Ma; Fig. 9, 10; Table 1), indicating that deposition of the basal Clematis at this locality occurred after ca. 227 Ma, which is stratigraphically consistent with the age for the Upper Arcadia Formation.

4. Discussion

5.1 Maximum depositional age (MDA) comparisons

5.1.1 Sampling strategy and Kernel Density Estimation (KDE) context

To maximize the robustness of MDAs, we first tested whether the zircon picking strategy shifts the youngest age modes and grain yields. We evaluated whether zircon selection influences the youngest age modes using paired splits from Taroom 14 (Fig. 5). A targeted sampling, favouring smaller, blocky, euhedral–subhedral grains with short-prismatic to equant habit and clear oscillatory zoning, yields a younger coherent mode (KDE peak ca. 241 Ma) (Fig. 5A, B). A random sampling shows a broader range of morphologies and grain sizes and yields an older dominant mode (KDE peak at ca. 252 Ma) (Fig. 5C, D). Within the ≤280 Ma window, the random sampling produced 107 concordant grains (62 Triassic), including 26 <245 Ma and 11 <240 Ma; the targeted sampling produced 91 concordant grains (60 Triassic), including 42 <245 Ma and 24 <240 Ma. Expressed as proportions of concordant grains, the targeted split enriches the youngest populations (<245 Ma: ca. 46% vs. ca. 24%; <240 Ma: ca. 26% vs. ca. 10%), indicating greater effectiveness in capturing near-depositional grains.

A second paired experiment in the Rewan-1 core shows the same behaviour (Fig. 5E, F). The targeted split yields 43 Triassic grains, of which 35 are younger than 245 Ma and 21 younger than 240 Ma, with KDE peaks at ca. 233 Ma and 242 Ma (Fig. 5E). The corresponding random split contains 31 Triassic grains, with only 13 <245 Ma and 6 <240 Ma, and its youngest major mode is shifted to ca. 248 Ma (Fig. 5F). Expressed as proportions of Triassic grains, the targeted selection contains ~81% <245 Ma and ~49% <240 Ma, compared with ~42% and ~19% in the random subset. These results further demonstrate that targeted picking systematically enriches the youngest, near-depositional Triassic zircon populations.

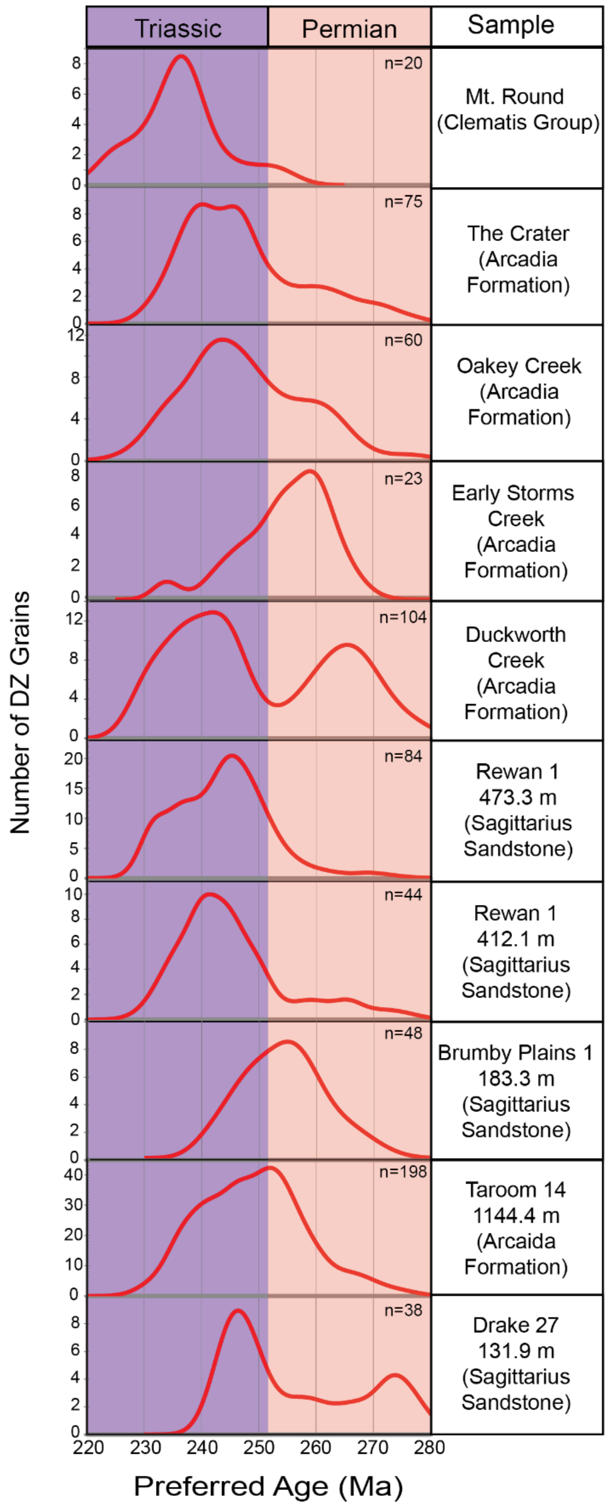

Figure 9. *Kernel density estimates of concordant detrital-zircon ages between 220–280 Ma for each sample. Curves are scaled to Number of DZ Grains (y-axis) vs Preferred Age (Ma) (x-axis); annotated labels mark modal peaks. Background shading denotes Triassic (purple) and Permian (pink); n gives the number of concordant grains within the window.*

Across the entire dataset, we use kernel density estimates (KDEs), which plot probability density curves of concordant U–Pb ages between 220 and 280 Ma, to identify the youngest coherent modes and compare samples (Vermeesch, 2012; Coutts et al., 2019; Fig. 9). Most samples display Triassic-peaked spectra with youngest modes between about 236 and 246 Ma. Examples include Mt. Round at about 236 Ma, The Crater at about 239 Ma, Oaky Creek at about 244 Ma, Duckworth Creek at about 242 Ma, Rewan-1 at 473.3 m at about 245 Ma, Rewan-1 at 412.1 m at about 241 Ma, and Drake-27 at about 246 Ma (Fig. 9). Other samples retain Permian-peaked distributions, including Taroom 14 at approximately 252

Ma, Brumby Plains-1 at about 255 Ma, and Early Storms Creek at about 257 Ma. We use these spectra as context for MDA selection. The youngest KDE modes identify coherent young populations, but KDE peaks do not substitute for formal maximum depositional constraints and can be biased by sampling density or smoothing choices. This observation aligns with the findings of Tucker et al. (2013), who evaluated the "youngest graphical peak" (YPP) approach in their Winton Formation (Eromanga Basin, Queensland, Australia) study and demonstrated that youngest peak ages consistently yield the oldest apparent MDAs and are much less sensitive for constraining true depositional ages. They recommended excluding YPP from comparative analyses due to this insensitivity and its tendency to overestimate depositional timing. Consistent with those conclusions we use KDE modes only for visual context and do not treat youngest peak or other graphical methods as quantitative MDA estimators in this study (Tucker et al., 2013; Dickinson & Gehrels, 2009; Coutts et al., 2019; Vermeesch, 2021).

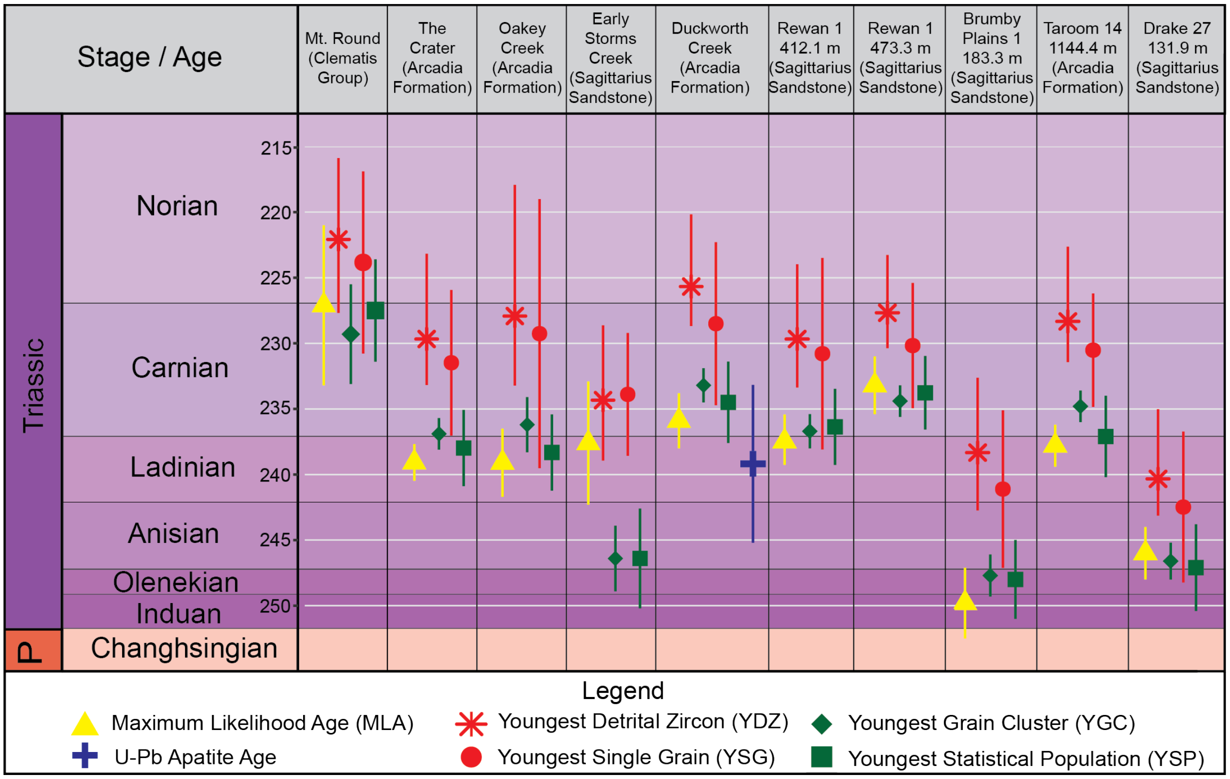

Figure 10. *Maximum depositional age (MDA) estimates for detrital zircon samples from outcrop and core localities in the northern Bowen Basin, plotted by sample name along the x axis and age (Ma) along the y axis. Background colours denote Permian and Triassic stages (Changhsingian through Norian), with stage boundaries shown as horizontal lines. Symbols indicate MDA metrics and the apatite minimum age: maximum likelihood age (MLA, yellow triangles), youngest detrital zircon (YDZ, red asterisks), youngest grain cluster (YGC, green diamonds), youngest single grain (YSG, red circles), youngest statistical population (YSP, green squares), and U Pb apatite age where available (blue crosses, Duckworth Creek). Error bars represent 2σ uncertainties for each age estimate.*

5.1.2 Sensitivity to discordance filtering Duckworth Creek case study

To assess how discordance filtering influences MDA estimates, we recalculated the Arcadia Formation sandstone at Duckworth Creek using three common discordance thresholds for detrital samples (≤15%, ≤10%, ≤5%; Table 2). All calculations are based on the same 301 analyses; only the number of concordant grains varies with the filter (172, 144, and 89, respectively). The results highlight systematic shifts in the youngest-age estimators and clarify why we adopt a 10% discordance filter for detrital zircon samples.

Duckworth Creek Discordance Filter	No. Analyses	YSG (Youngest Single Grain)	YDZ (Gehelles)	YGC (±2σ)	YSP (Coutts et al, 2019)	MLA (Veermesch, 2021)
15%	301 analyses; 172 Concordant	218.8 ± 5.63; 11.55% Discordant	218.67 +4.1/-6.0 Ma	225.5 ± 3.2; MSWD 1.8; 9 grains	223.0 ± 4.4 Ma; MSWD= 1.4; 5 grains	231.1 ± 2.9 Ma
10%	301 analyses; 144 Concordant	228.5 ± 6.21; 1.25% Discordant	225.67 +3/-5.5 Ma	233.2 ± 1.3; MSWD 0.77; 24 grains	234.5 ± 3.1 Ma; MSWD= 0.98; 31 grains	235.9 ± 2.0 Ma
5%	301 analyses; 89 Concordant	228.5 ± 6.21; 1.25% Discordant	226.33 +3.4/-5.6 Ma	234.5 ± 1.9; MSWD 1.5.; 19 grains	233.4 ± 1.6 Ma; MSWD= 1.05; 16 grains	232.8 ± 3.1 Ma

***Table 2**. Summary of detrital zircon U Pb MDA results for the Arcadia Formation sandstone at Duckworth Creek calculated under three discordance thresholds (15, 10 and 5 percent). For each filter, the table lists the number of analyses and concordant grains, and the corresponding youngest single grain (YSG), youngest detrital zircon (YDZ), youngest grain cluster (YGC, ±2σ), youngest statistical population (YSP) and maximum likelihood age (MLA) estimates*.

At a 15% discordance threshold, the youngest metrics yield markedly young apparent ages: YSG and YDZ fall at ca. 219 Ma, and cluster-based estimators (YGC2σ, YSP) at ca. 223–226 Ma (Table 2). These values are likely younger than any plausible depositional age of the Arcadia Formation and sit well below the coherent Triassic modes observed in KDEs (Fig. 9). The corresponding clusters are small (9–5 grains) and moderately over-dispersed (MSWD ≈ 1.4–1.8). We interpret these grains as a small population of anomalously young analyses produced by minor Pb-loss in zircons that pass a permissive discordance filter, rather than as a genuine near-depositional age component. However, the MLA at 15% discordance (231.1 ± 2.9 Ma) is less affected by these few anomalously young grains, displaying the reduced sensitivity of the likelihood-based estimator to Pb-loss related outliers (Coutts et al., 2019; Vermeesch, 2021).

Tightening the filter to 10% discordance removes the youngest, most discordant analyses and stabilizes the youngest coherent population. The YGC2σ and YSP estimators converge at ca. 233–235 Ma with improved MSWD values (≈0.8–1.0) and larger cluster sizes (24–31 grains), while the MLA increases to 235.9 ± 2.0 Ma (Table 2). Further tightening to 5% discordance reduces the number of concordant grains to 89, slightly shifts the MLA to 232.8 ± 3.1 Ma, and increases the uncertainties on the cluster-based estimates. We regard the 5% filter as overly restrictive for these detrital datasets because it sacrifices a substantial fraction of otherwise acceptable Triassic grains and does not yield a demonstrably more robust youngest population.

On this basis, we apply a 10% discordance filter to detrital zircon MDAs across the stratigraphic successions of both the Rewan Group and the Clematis Group. For Duckworth Creek, this threshold rejects grains that are most plausibly affected by minor Pb-loss, yields well-behaved youngest clusters (YGC2σ, YSP) of adequate size, and produces an MLA that is consistent with independent chronostratigraphic constraints and with regional Triassic age distributions. Table 2, therefore, illustrates both the susceptibility of single-grain and simple cluster-based MDAs to Pb-loss under permissive filtering, and the relative stability of the MLA estimator when discordance thresholds are chosen conservatively.

5.1.3 Behaviour of MDA estimators

We next evaluate several commonly applied metrics for maximum depositional age (MDA) determination, including the youngest single grain (YSG), youngest detrital zircon (YDZ), youngest grain cluster at 2σ (YGC2σ), youngest statistical population (YSP), and maximum likelihood age (MLA), in order to guide the selection of defensible maximum depositional age constraints in siliciclastic successions (Dickinson and Gehrels, 2009; Tucker et al., 2013; Coutts et al., 2019; Herriott et al., 2019; Vermeesch, 2021) (Fig. 10). Across our dataset, these estimators exhibit a consistent rank order from youngest to oldest: YSG or YDZ < YGC2σ ≈ YSP < MLA (Coutts et al., 2019; Vermeesch, 2021). Across all samples, the single grain estimators yield the youngest apparent ages, the cluster-based estimators give intermediate ages, and the MLA returns the oldest values. We therefore adopt MLA as the primary MDA estimator for the Rewan Group and use YGC2σ and YSP as internal checks on this choice. YSG and YDZ are reported as minimum bounds only and are not interpreted as depositional ages. Any detrital zircon MDA represents a maximum age constraint, so the true depositional age of the unit must be no older than its youngest zircons (Dickinson and Gehrels, 2009; Coutts et al., 2019).

MLA is preferred because it combines several grains and their uncertainties into a single estimate, rather than relying on one or two outliers, and is therefore less sensitive to anomalously young analyses produced by minor Pb loss or large analytical uncertainties. By using the distribution of the youngest several grains, the MLA reduces the influence of such outliers. Published simulation work and case studies show that MLA-based MDAs often agree more closely with independent ages for volcanic units than single-grain or simple cluster-based metrics, and our results are consistent with that behaviour where ash bed ages are available (Coutts et al., 2019; Vermeesch, 2021). Reporting YGC2σ and YSP alongside MLA allows readers to see how the youngest cluster compares with the likelihood solution and provides a simple internal sensitivity check (Dickinson and Gehrels, 2009; Herriott et al., 2019).

However, we do not apply MLA automatically. An MLA based on the youngest cluster is not reliable when that cluster is very small or statistically poorly behaved, for example when it contains fewer than three grains or has a mean square of weighted deviates (MSWD) greater than 2 without geological justification (Vermeesch, 2021). We favour the younger cluster-based estimate as the more plausible maximum depositional age when MLA conflicts with a secure external age, such as a U-Pb age from a volcanic ash or a tightly constrained fossil assemblage, but YGC2σ or YSP agrees with that external age within uncertainty. When field or sedimentological evidence indicates extensive reworking or mixing from older strata, the youngest zircons are likely to be recycled rather than syndepositional. In these cases, we again prefer the cluster-based MDA as a better approximation of depositional timing and still report MLA for completeness. These rules keep MLA use tied to geological context rather than to a single default approach.

5.2 Revised Stratigraphy of the Triassic Bowen Basin

New U–Pb constraints from Permian tuffs and Triassic detrital zircons allow us to refine the chronostratigraphy of the northern Bowen Basin across the Denison Trough, Comet Ridge, and northern Taroom Trough (Fig. 11; Table 1). Throughout this section, MDAs refer to MLA values calculated at a 10% discordance threshold (Section 5.1), and quoted uncertainties are 2σ. Permian tuff ages are treated as absolute depositional ages that anchor the base of the Triassic succession in each domain.

5.2.1 Denison Trough (back-bulge)

The upper Permian ash at Rewan-1 (563.1 m; Bandanna Formation tuffaceous mudstone) yields a Concordia $^{206}Pb/^{238}U$ age of 251.4 ± 1.9 Ma, placing the top of the coal-measure succession in the latest Changhsingian–earliest Induan (Fig. 7; Table 1). This result agrees with high-precision CA–ID–TIMS zircon ages obtained for correlative late Permian tuffs elsewhere in the Bowen and the adjacent Galilee basins, including 252.24 ± 0.36 Ma at the top of the Bandanna Formation and 252.81 ± 0.07 Ma for the basin-wide Yarrabee Tuff (McKellar et al., 2015; Nicoll et al., 2015; Ayaz et al., 2016; Metcalfe et al., 2024). Together, these ages define a robust latest Permian reference surface immediately beneath the Rewan Group in the Denison Trough back-bulge.

The overlying Rewan Group MDAs in the Denison Trough are uniformly Middle–early Late Triassic. The Sagittarius Sandstone in Rewan-1 yields MLA-based MDAs of 237.7 ± 2.5 Ma at 412.1 m and 233.2 ± 2.2 Ma at 473.5 m (Table 1). Arcadia Formation outcrops at The Crater, and Oaky Creek return MLAs of 239.0 ± 1.6 Ma and 239.2 ± 3.2 Ma, and the basal part of the Clematis Group at Mount Round yields an MLA of 227.4 ± 6.1 Ma. These data show that Triassic strata preserved in the Denison Trough post-date ca. 239–233 Ma, whereas the underlying Bandanna ash constrains the end of coal-measure deposition at 251–252 Ma. The slightly older MDAs for the Arcadia Formation at The Crater and Oakey Creek, compared to the lower Sagittarius Sandstone in Rewan-1, are best interpreted as conservative maxima. They most likely reflect lower proportions of concordant Triassic grains and earlier, less targeted grain picking in those outcrops, rather than a real reversal in stratigraphic age, and are consistent with the younger Arcadia MDA at Duckworth Creek and the picking-strategy effects shown in Section 5.1.1.

The age difference between the latest Permian ash at Rewan-1 (251–252 Ma) and the overlying Middle to early Late Triassic MDAs for the Rewan Group (ca. 239–233 Ma) implies a substantial interval between the latest Permian coal-swamp deposition and the onset of preserved Rewan Group sedimentation in the Denison Trough. Using the Rewan-1 ash (251.4 ± 1.9 Ma) and the oldest overlying Triassic MDAs (Sagittarius Sandstone at 412.1 m: 237.7 ± 2.5 Ma; Arcadia Formation at ca. 239 Ma), the Denison gap is at least ~12–15 Myr (Fig. 11). Considering the younger internal MDAs (e.g., Sagittarius Sandstone at 473.5 m: 233.2 ± 2.2 Ma) and the Clematis Group MDA (227.4 ± 6.1 Ma) indicates that the total interval lacking preserved strata may be longer. However, because MDAs are maximum constraints, we treat these values as upper bounds on the true duration of non-deposition and/or erosion. Lower concordance in some Arcadia Formation outcrops in the Denison Trough (e.g., 39–58% concordant grains at <10% discordance) can preferentially exclude the youngest zircon analyses and bias conservative MDAs slightly older; however, even allowing for such effects, there is no evidence for Olenekian or early–middle Anisian deposition in the preserved Denison Trough section.

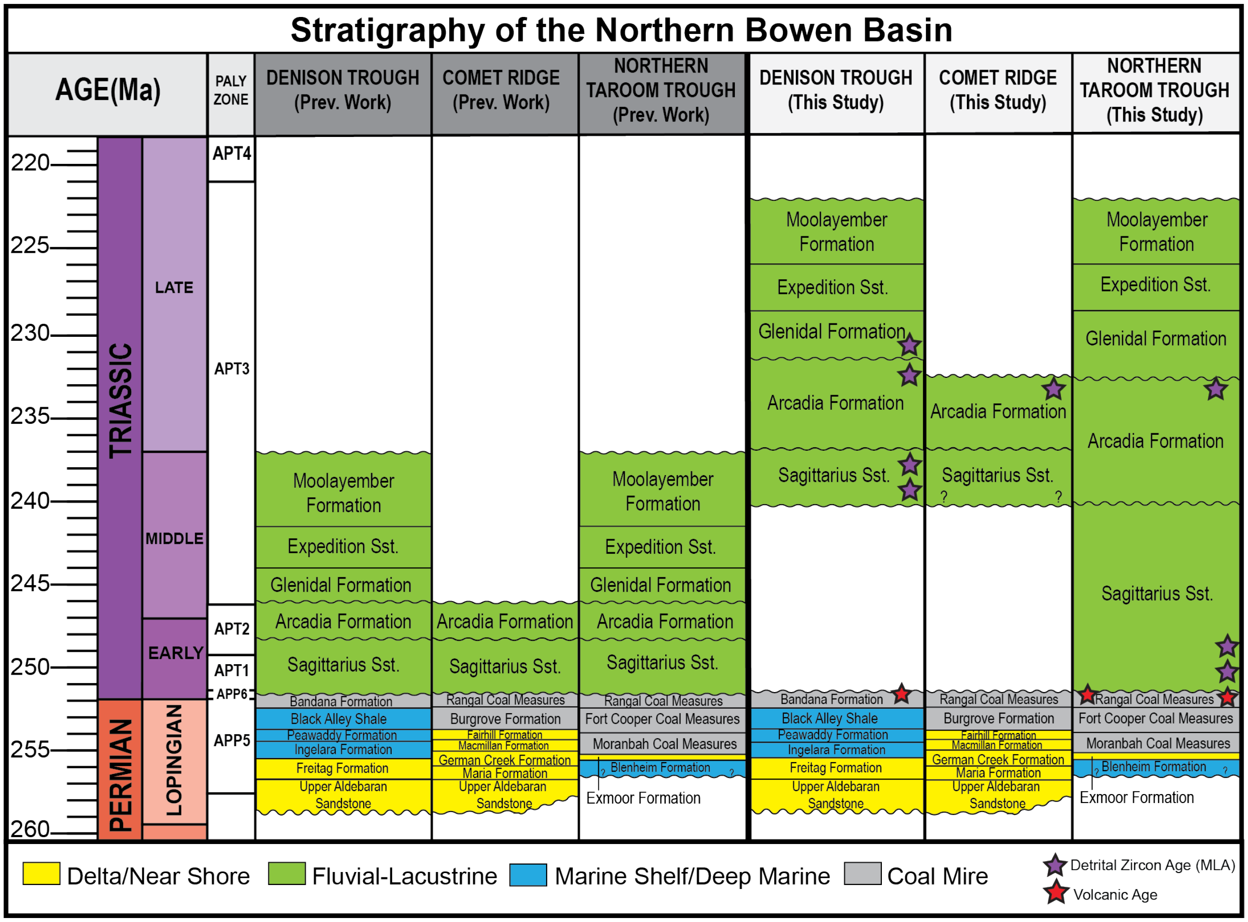

__Figure 11.__ Comparative stratigraphic framework for the northern Bowen Basin showing Late Permian to Triassic formations before (left three columns) and after (right three columns) following incorporation of new maximum-depositional-age constraints. Columns are organized by structural domain: Denison Trough, Comet Ridge, and Northern Taroom Trough. The vertical axis is age in Ma with corresponding palynozones. Coloured fills denote dominant depositional facies: delta/nearshore (yellow), fluvial–lacustrine (green), marine shelf/deep marine (blue), and coal-smire (grey). Purple stars mark detrital-zircon MLA ages and red stars volcanic-ash ages that inform revised unit boundaries for the Sagittarius Sandstone, Arcadia Formation, Glenidal Formation, and overlying units.

5.2.2 Taroom Trough (foredeep)

In the northern Taroom Trough, two Permian tuffs provide tightly constrained age anchors immediately beneath the Triassic red beds. A tuff in the Rangal Coal Measures at Drake NS27 (275.6 m) yields a Concordia age of 252.6 ± 1.2 Ma, and the tuffaceous bed at Theodore NS150 (171.5 m), directly above the last major coal, gives 251.8 ± 0.6 Ma (Fig. 11; Table 1). These ages fall within the narrow 252–253 Ma window defined by regional CA–ID–TIMS ages for the Yarrabee/Kaloola volcanic system and allied upper Permian markers (e.g., Yarrabee Tuff 252.81 ± 0.07 Ma; McKellar et al., 2015; Nicoll et al., 2015; Ayaz et al., 2016; Metcalfe et al., 2024), supporting their correlation as basin-wide reference horizons at the top of the coal measures.

The overlying Rewan Group in the Taroom foredeep shows progressive younging of MLAs without requiring a major hiatus at our sampling resolution. Along the western margin of the foredeep, the Sagittarius Sandstone at Brumby Plains1 (183.3 m) yields an MLA of 249.8 ± 2.7 Ma, whereas the mid-successional Sagittarius Sandstone at Drake NS27 (131.9 m) returns 245.9 ± 1.9 Ma; both ages fall within the Olenekian to late Anisian (Fig. 11; Table 1). Farther east and structurally higher in the basin centre well Taroom 14, an Arcadia Formation sandstone at 1144.4 m immediately beneath the Clematis Group, yields an MLA of 237.8 ± 1.6 Ma, corresponding to a late Ladinian–earliest Carnian MDA. The Taroom Trough data indicate relatively continuous accommodation and deposition from just above the latest Permian tuffs through the Early and Middle Triassic, with no evidence for a Denison scale hiatus.

Comet Ridge occupies an intermediate structural position (forebulge) between the Denison Trough backbulge to the west and the Taroom Trough foredeep to the east during the Triassic. The only dated locality in this domain is the Arcadia Formation sandstone at Duckworth Creek, which yields an MLA of 235.9 ± 2.0 Ma (early Carnian; Table 1). Detrital apatite from the same tuffaceous sandstone forms a coherent array on a Tera–Wasserburg diagram, defining a lower intercept age of 239.3 ± 6.6 Ma (Fig. 8). All apatite analyses come from a single volcaniclastic sandstone bed and define a coherent regression with low MSWD. We therefore interpret the lower intercept age as a corroborative minimum that is consistent with the zircon-based MDA for the same horizon, rather than as an independent depositional age.

At the basin scale, the new ages show that the lower Rewan Group contact is time-transgressive from west to east (Fig. 11). In the Denison Trough, latest Permian ash beds (ca. 251–252 Ma) lie directly beneath Middle–early Late Triassic MDAs (ca. 239–233 Ma), implying a significant interval of non-deposition and/or erosion at the base of the Rewan Group. In contrast, in the Taroom Trough foredeep, the same latest Permian tuffs are overlain by a succession that youngs smoothly from Olenekian to late Anisian Sagittarius Sandstone MDAs and then to late Ladinian–earliest Carnian Arcadia Formation MDAs, with no large stratigraphic break suggested by the detrital record. Comet Ridge, with its early Carnian Arcadia Formation MDA and corroborative apatite minimum age at Duckworth Creek, lies between these endmembers both geographically and temporally.

Expressed numerically, the Denison Trough gap runs from the Rewan 1 Bandanna Formation ash at 251.4 ± 1.9 Ma to the oldest overlying Triassic MDAs between about 239 and 237.7 Ma, which implies a minimum hiatus of roughly 12 to 15 Myr that may be longer if younger MDAs are included. This estimate should be regarded as a minimum as MDAs are upper bounds on depositional age, and conservative discordance filtering may slightly bias them toward older ages by preferentially removing the youngest grains. By comparison, the Taroom Trough record shows stepwise younging from latest Permian tuffs (252.6 to 251.8 Ma) through Olenekian to late Anisian Sagittarius Sandstone MLAs (249.8 to 245.9 Ma) and then to late Ladinian to earliest Carnian Arcadia Formation MLAs (237.8 Ma). This progression is internally consistent and does not require a substantial hiatus at the resolution of our dataset. These contrasts (Fig. 11) are best explained by accommodation that developed at different times in each domain; the Taroom Trough foredeep began subsiding and trapping sediment earlier and for longer, whereas significant back bulge fill in Denison Trough started later and is more condensed.

5.3 Tectonic Implications of the Updated Geochronology Framework

The new U–Pb dating constraints allow us to integrate basin evolution with the timing of the Hunter–Bowen Orogeny. The onset of slab advance at ca. 265 Ma marks the beginning of foreland loading and thrust propagation outboard of the New England Orogen, establishing the template for flexural subsidence and basin partitioning (Jessop et al., 2019; Fig. 12A). Absolute ages from Permian tuff beds immediately below the Triassic succession provide absolute ages at the top of the latest Permian Bandanna Formation (and co-eval strata) to this framework at ca. 252 to 251 Ma and demonstrate that accommodation in the northern Bowen Basin initiated against a latest Permian datum consistent with prior stratigraphic syntheses (Grech, 2001; Korsch et al., 2009; Decelles, 2012; Fig. 7).

During the foreland loading phase, ca. 255 to 240 Ma, subsidence was focused in the Taroom Trough (foredeep), and the Denison Trough behaved largely as a back-bulge bypass (Catuneanu, 2004), a pattern that is captured by our earliest Triassic MDAs from foredeep sandstone bodies. The Sagittarius Sandstone yields MLA-based MDAs of 249.8 ± 2.7 Ma at Brumby Plains-1 and 245.9 ± 1.9 Ma at Drake 27, which require persistent early accommodation and efficient sediment trapping in the Taroom Trough (Fig. 12B). These values are coherent with a classic flexural foreland system in which the load concentrated subsidence is on the cratonic side of the orogenic front, while the back-bulge region remain sediment starved (Grech, 2001; Korsch et al., 2009; Decelles, 2012). The volcanolithic petrofacies and abundant pyroclastic detritus in Upper Permian to Lower Triassic sandstones are compatible with sustained arc-derived sediment supply to the foredeep during this phase (Michaelsen and Henderson, 2000).

By ca. 240 to 230 Ma, dynamic subsidence related to slab kinematics appears to have overprinted the flexural signal, promoting the transition from bypass to active fill in the Denison

Trough (Fig. 12C). Within the Rewan-1 core in Denison Trough, MLA-based MDAs of 237.7 ± 2.5 Ma at 412.1 m and 233.2 ± 2.2 Ma at 473.5 m, the latter approximately 23 m above the last Permian coal from the Bandanna Formation, document the timing of renewed accommodation and the encroachment of Triassic fluvial systems into the back-bulge. Outcrop Arcadia Formation samples in Denison Trough reinforce this picture with MDAs of 237.6 ± 4.7 Ma at Early Storms Creek, 239.2 ± 3.1 Ma at Oaky Creek, and 239.0 ± 1.6 Ma at The Crater. In comparison, the forebulge at Comet Ridge yields an age of 235.9 ± 2.0 Ma at Duckworth Creek. In the Taroom Trough, the top of the Arcadia Formation is 237.8 ± 1.6 Ma, indicating that the upper part of the Arcadia Formation is chronostratigraphically equivalent across foredeep, forebulge, and back-bulge settings within uncertainty. Taken together, these data imply a lag of approximately 8 to 12 million years between the earliest foredeep accumulation and the onset of widespread back-bulge fill, consistent with along-strike variability in effective flexural rigidity and changes in dynamic support associated with asymmetric rollback and arc migration (Li et al., 2012, 2015; Milan et al., 2021).

The Clematis Group records waning foreland loading and reduced flexural accommodation, marking the shift toward the Late Triassic contractional phase that deformed the Bowen–Sydney foreland system (Jenkins et al., 2002; Korsch et al., 2009). Our Mount Round MDA of 227.4 ± 6.1 Ma places the Clematis Group within a late Carnian to early Norian window and indicates that major fluvial aggradation outlasted the main Sagittarius–Arcadia phase (Fig. 12D). After the accumulation of the Clematis Group and the Moolayember Formation, the basin experienced structural inversion, followed by post-210 Ma peneplanation and the development of distributed extensional basins during slab retreat (Fig. 12E). These transitions align with regional accounts of contractional climax, subsequent reorganization, and late orogenic collapse across the

Tasmanides, and they remain compatible with a flexural foreland system that later incorporated a strong dynamic component due to slab processes and arc migration (Korsch et al., 2009; Hoy et al., 2018; Jessop et al., 2019; Hoy, 2020; Campbell et al., 2022).

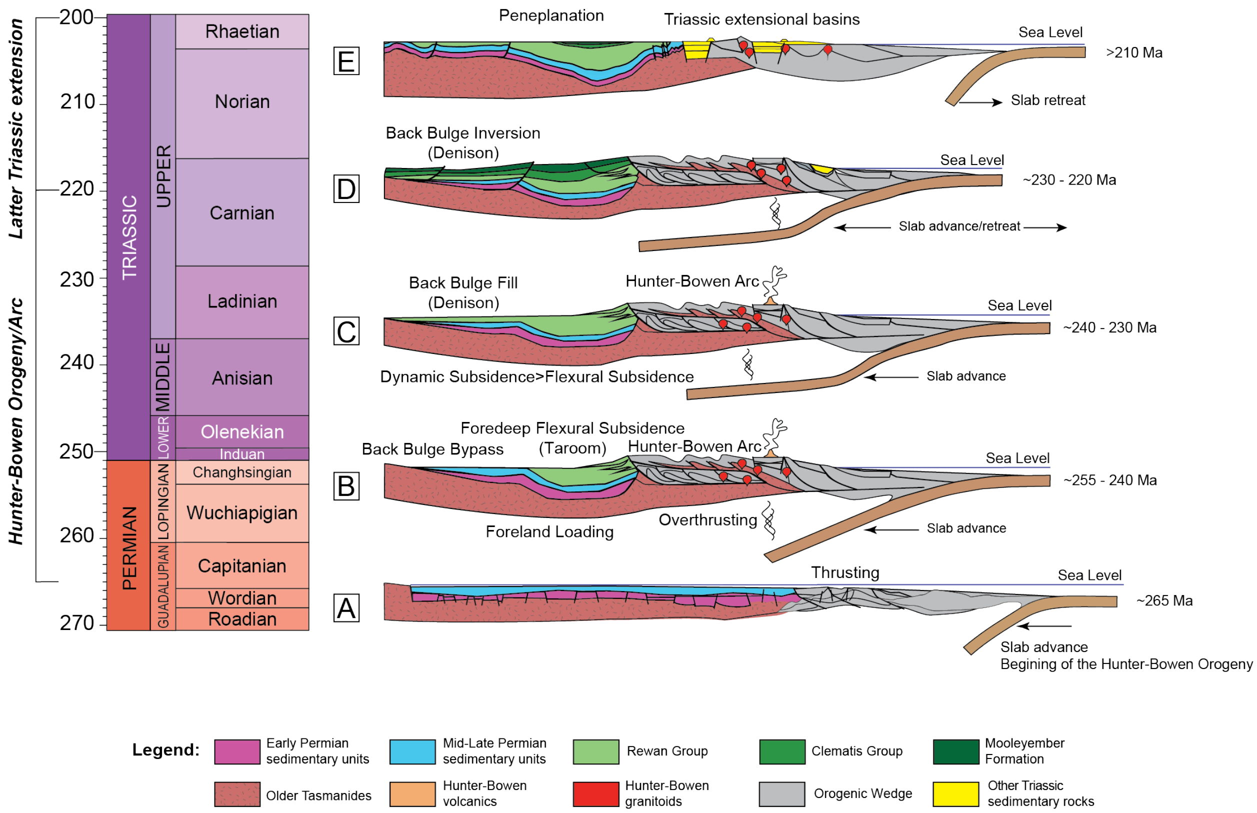

Figure 12. *Stylized tectono-stratigraphic cross-section showing how the Hunter–Bowen Orogeny shaped the Bowen Basin through time (Permian–Triassic column at left) modified and adapted from (Sliwa et al., 2018; Jessop et al., 2019) Panels A–E illustrate the progression from slab advance and foreland loading with thrusting (A), to flexural foreland development with foredeep subsidence in the Taroom Trough and back-bulge bypass in the Denison Trough (B), followed by continued arc magmatism and back-bulge fill (C), back-bulge inversion (D), and finally Late Triassic extensional basins during slab retreat (E). Coloured units highlight the Rewan Group, Clematis Group, and Moolayember Formation relative to the older Tasmanides, orogenic wedge, and arc volcanics/granitoids (legend); schematic, not to scale.*

5.4 Implications for Triassic Vertebrate Fossil Assemblages and Biodiversity Trends

Two globally significant vertebrate fossil-bearing localities within the Arcadia Formation, “The Crater” in the Denison Trough (Fig. 1B; 3D) and Duckworth Creek on Comet Ridge (Fig.

1A; 3E), have long been regarded as key reference sites for Early Triassic continental faunas in eastern Gondwana (Warren et al., 2001). Hosting diverse temnospondyl-dominated assemblages together with rarer amniotes and fishes, these sites have generally been regarded as earliest Triassic (Induan–Olenekian) in age based on stratigraphic position and palynology (Warren, 1981; Northwood, 1999). Thus, closely tied to the immediate aftermath of the end-Permian mass extinction (Benton, 2016, 2018; Romano et al., 2020). As such, the Arcadia Formation vertebrate assemblages have been incorporated into discussions on post-extinction recovery, faunal turnover and biogeographic patterns in Early Triassic continental ecosystems across Pangaea (Warren, 1980, 1981, 1985; Warren and Black, 1985; Warren and Hutchinson, 1987; Damiani and Warren, 1997; Warren and Marsicano, 1998, 2000; Northwood, 1999, 2005; Warren et al., 2001, 2006, 2011; Nield et al., 2006; Rozefelds et al., 2011).

The new detrital zircon U–Pb MDAs presented here substantially revise the temporal context of these assemblages, and warrants an extensive review of their contribution towards our understanding of Triassic continental ecosystems. Maximum likelihood ages place "The Crater" at 238.9 ± 1.4 Ma (late Ladinian) and Duckworth Creek at 235.9 ± 2.1 Ma (early Carnian). These values are maximum depositional ages and are expected to be equal to or older than the true depositional ages, but within our dataset, they provide the most consistent estimate of relative timing. These results indicate that both assemblages are late Middle–early Late Triassic rather than earliest Triassic, and that the two sites are potentially not coeval. The ca. 3–5 Myr age offset is supported by the absence of documented species-level overlap within the vertebrate fossil record between the two localities (Warren, 1981, 1985; Warren and Black, 1985; Warren and Hutchinson, 1987; Damiani and Warren, 1997; Warren and Marsicano, 1998, 2000; Northwood, 1999; Warren et al., 2001, 2011; Nield et al., 2006; Rozefelds et al., 2011; but see Hamley et al., 2021). Rather than representing a single, time-equivalent fauna, The Crater and Duckworth Creek now appear to sample different stages of Middle–Late Triassic ecosystem development in the northern Bowen Basin. However, it remains possible that the lack of taxonomic overlap is the result of geography and/or environmental factors, providing a different set of habitats at each locality.

The revised ages also bear directly on interpretations of climatic and paleoenvironmental conditions. The interval between ca. 239 – 236 Ma spans the onset of the Carnian Pluvial Episode (CPE) (Benton et al., 2018; Corso et al., 2020). This episode is marked by higher rainfall, increased runoff, and associated biotic and sedimentary change in many basins (Benton et al., 2018; Corso et al., 2020; Zhao et al., 2025). Within our chronostratigraphic framework, The Crater predates the main phase of CPE humidification, whereas Duckworth Creek overlaps its early development. Consequently, any comparison of facies, taphonomy or vertebrate ecology between The Crater and Duckworth Creek should acknowledge that the ages are MDAs and that small differences between them may include effects of sediment routing, the depositional environment and sampling, not only true time differences. The main implication of our new ages is that the upper Arcadia vertebrate assemblages no longer fall in the earliest Triassic but in the late Ladinian to early Carnian. They should not be used as evidence for earliest Triassic recovery and instead need to be considered in work on Middle–Late Triassic extinction, turnover and diversity, including studies of the Carnian Pluvial Episode and the rise of modern terrestrial ecosystems. This gives a new opportunity to use the Bowen Basin as a record of how CPE-age climate change and basin evolution affected vertebrate communities in the southeastern part of Pangaea (Tucker and Benton, 1982; Zhu et al., 2019; Chapman et al., 2022).

The new ages also place the Arcadia Formation vertebrate assemblages in the same Middle–Late Triassic interval as several important continental successions, including the Molteno

Formation at the base of the Stormberg Group in the Karoo Basin, the Ischigualasto Formation in northwestern Argentina, the Lossiemouth Sandstone Formation in the Elgin area of Scotland, the Madygen Formation in Kyrgyzstan and the Popo Agie Formation in the western United States (Anderson et al., 1998; Martínez et al., 2012; Hancox et al., 2020; Fitch et al., 2023; Foffa et al., 2024). These units are widely used to reconstruct Carnian to early Norian terrestrial environments and faunas. Placing the Arcadia record in this time frame allows direct comparison with this global set of basins when assessing patterns of vertebrate diversity and environmental change.

6. Conclusions

Following a comprehensive sampling of the Sagittarius Sandstone and Arcadia Formation, we demonstrate high-density U–Pb zircon datasets (around 300 analyses per sandstone), anchored to the latest Permian ash beds at 252–251 Ma, that define a reproducible chronostratigraphic framework for the northern Bowen Basin, Queensland, Australia (Fig. 11; Table 1). Sagittarius Sandstone MDAs range from ca. 250–233 Ma, Arcadia Formation MDAs cluster between ca. 239–236 Ma, and the basal part of the Clematis Group at Mount Round yields an MDA of 227.4 ± 6.1 Ma. Together with the Permian tuffs, these ages resolve ambiguity left by palynology-only schemes and allow consistent intra- and inter-basinal correlation of Triassic strata.

The base of the Rewan Group is time-transgressive across the basin. In the Denison Trough (backbulge), latest Permian ash from the Bandanna Formation at Rewan 1 (251.4 ± 1.9 Ma) is overlain directly by late Middle–early Late Triassic Sagittarius Sandstone and Arcadia Formation MDAs between ca. 239 and 233 Ma, implying a Denison Trough chronostratigraphic unconformity of at least about 12–15 Myr. In the Taroom Trough (foredeep), by contrast, deposition appears relatively continuous from latest Permian tuffs (252.6–251.8 Ma) through Olenekian to late

Anisian Sagittarius Sandstone MDAs (249.8–245.9 Ma) and into late Ladinian to earliest Carnian Arcadia Formation MDAs (237.8 Ma), with Comet Ridge, represented by the Arcadia Formation sandstone at Duckworth Creek (MLA 235.9 ± 2.0 Ma), occupying an intermediate position. This pattern is most simply explained by earlier and more sustained accommodation in the foredeep and by a more condensed, locally erosional Triassic fill in the Denison Trough.

The new age framework also substantially revises the timing of Arcadia Formation vertebrate localities. Maximum likelihood MDAs place The Crater at 238.9 ± 1.4 Ma (late Ladinian) and Duckworth Creek at 235.9 ± 2.0 Ma (early Carnian), and a detrital apatite lower intercept age of 239.3 ± 6.6 Ma from Duckworth Creek provides an independent minimum constraint consistent with the zircon MDA. These sites are therefore Middle–early Late Triassic, not earliest Triassic, and they are unlikely to be the same age. The 3–5 Myr difference between their MDAs gives a clearer time frame for future paleoenvironmental comparisons and argues against treating the two assemblages as a single pooled fauna.

Finally, our workflow combines large detrital zircon datasets, conservative discordance filters, clear rules for MDA selection and checks against ash-bed and apatite ages. In this framework, MLA at 10% discordance is the primary MDA estimator, YGC2σ and YSP are internal checks, and YSG/YDZ are used only as minimum bounds. Agreement between these metrics and independent age anchors supports our age interpretations and provides a simple template for refining chronostratigraphy and tectono-stratigraphic models in other siliciclastic basins.

Acknowledgements

We gratefully acknowledge the Geological Survey of Queensland and the team at Zillmere for providing access to the Drake NS 27, Taroom 14, Rewan-1 and Theodore NS 150. We also acknowledge the use of facilities and technical support from the Queensland Core Library (GSQ, Zillmere). We also thank Santos and Mel Wilkinson for permission to sample the Brumby Plains 1 core, and the landholders at Duckworth Creek, Oaky Creek and Early Storms Creek for access to outcrop localities. We also thank the Department of the Environment, Tourism, Science, and Innovation for access to "The Crater" and Mt. Round in the Seracold State Forest. We respectfully acknowledge the Traditional Owners past, present and emerging of the Country on which this work was conducted, including Bidjara, Gayiri, Gabalara, Gangulu and Biri Country.

Detrital zircon separation was carried out in the JCU Mineral Separation Laboratory; we thank Huiqing Huang for expert assistance and training. U–Pb analyses were performed at the Advanced Analytical Centre, James Cook University—special thanks to Huiqing Huang and the AAC staff for their guidance with the LA-ICP-MS system and data reduction workflows. This work was funded by the Queensland Museum, with additional support from James Cook University's College of Science and Engineering research fund. M.S. is grateful to the Team of Dreams for insightful tips and discussions on Triassic stratigraphy.

References

Anderson, J. M., H. M. Anderson, and A. Cruickshank, 1998, Late Triassic ecosystems of the Molteno/Lower Elliot biome of southern Africa: Palaeontology, v. 41, p. 387–421.

Ayaz, S. A., S. Rodrigues, S. D. Golding, and J. S. Esterle, 2016, Compositional variation and palaeoenvironment of the volcanolithic Fort Cooper Coal Measures, Bowen Basin, Australia: International Journal of Coal Geology, v. 166, p. 36–46, doi:10.1016/j.coal.2016.04.007.

Babaahmadi, A., P. Brooks, and M. Grant, 2021, Post-orogenic structural style and reactivation in the northern Bowen Basin, eastern Australia: Australian Journal of Earth Sciences, v. 68, no. 2, p. 188–203, doi:10.1080/08120099.2020.1767206.

Baker, J. C., 1997, Green ferric clay in non-marine sandstones of the Rewan Group, southern Bowen Basin, eastern Australia: Clay Minerals, v. 32, no. 4, p. 499–506.

Barham, M., C. L. Kirkland, and A. D. Handoko, 2022, Understanding ancient tectonic settings through detrital zircon analysis: Earth and Planetary Science Letters, v. 583, p. 117425, doi:10.1016/J.EPSL.2022.117425.

Bashari, A., 2000, Petrography and clay mineralogy of volcanoclastic sandstones in the Triassic Rewan Group, Bowen Basin, Australia: Petroleum Geoscience, v. 6, no. 2, p. 151–163, doi:10.1144/petgeo.6.2.151.

Benton, M. J., 2018, Hyperthermal-driven mass extinctions: Killing models during the Permian-Triassic mass extinction: Royal Society Publishing, doi:10.1098/rsta.2017.0076.

Benton, M. J., 2016, The Triassic: Cell Press, p. R1214–R1218, doi:10.1016/j.cub.2016.10.060.

Benton, M. J., M. Bernardi, and C. Kinsella, 2018, The Carnian Pluvial Episode and the origin of dinosaurs: Journal of the Geological Society, v. 175, no. 6, p. 1019–1026, doi:10.1144/jgs2018-049.

Bernardi, M., F. M. Petti, and M. J. Benton, 2018, Tetrapod distribution and temperature rise during the Permian–Triassic mass extinction: Proceedings of the Royal Society B: Biological Sciences, v. 285, no. 1870, doi:10.1098/rspb.2017.2331.

Botha, J., and R. M. H. Smith, 2006, Rapid vertebrate recuperation in the Karoo Basin of South Africa following the End-Permian extinction: Journal of African Earth Sciences, v. 45, no. 4–5, p. 502–514, doi:10.1016/j.jafrearsci.2006.04.006.

Brakel, A. T., J. M. Totterdell, A. T. Wells, and M. G. Nicoll, 2009, Sequence stratigraphy and fill history of the Bowen Basin, Queensland: Australian Journal of Earth Sciences, v. 56, no. 3, p. 401–432, doi:10.1080/08120090802698711.

Brayard, A. et al., 2017, Unexpected Early Triassic marine ecosystem and the rise of the Modern evolutionary fauna: Science Advances, v. 3, no. 2, doi:10.1126/sciadv.1602159.

Cadman, S. J., L. Pain, and V. Vuckovic, 1998, BOWEN AND SURAT BASINS, Clarence-Moreton Basin, Sydney Basin, Gunnedah Basin and other minor onshore basins, Qld, NSW and NT.

Campbell, M. J., D. Hoy, G. Rosenbaum, C. Fielding, and C. M. Allen, 2022, The Onset of Gondwanide Orogeny in Eastern Australia: Insight From the Provenance of Syn-Orogenic Strata in the New England Orogen (Australia): Tectonics, v. 41, no. 2, doi:10.1029/2021TC006940.

Campbell, M. J., U. Shaanan, and C. Verdel, 2017, Fold-interference patterns in the Bowen Basin, northeastern Australia: Australian Journal of Earth Sciences, v. 64, no. 5, p. 577–585, doi:10.1080/08120099.2017.1334704.

Catuneanu, O., 2004, Retroarc foreland systems—evolution through time: Journal of African Earth Sciences, v. 38, no. 3, p. 225–242, doi:10.1016/J.JAFREARSCI.2004.01.004.

Chapman, T., L. A. Milan, I. Metcalfe, P. L. Blevin, and J. Crowley, 2022, Pulses in silicic arc magmatism initiate end-Permian climate instability and extinction: Nature Geoscience, v. 15, no. 5, p. 411–416, doi:10.1038/s41561-022-00934-1.

Chen, C., S. Qin, Y. Wang, G. Holland, P. Wynn, W. Zhong, and Z. Zhou, 2022, High temperature methane emissions from Large Igneous Provinces as contributors to late Permian mass extinctions: Nature Communications, v. 13, no. 1, doi:10.1038/s41467-022-34645-3.

Chu, D., J. D. Corso, W. Shu, H. Song, P. B. Wignall, S. E. Grasby, B. van de Schootbrugge, K. Zong, Y. Wu, and J. Tong, 2021, Metal-induced stress in survivor plants following the end-Permian collapse of land ecosystems: Geology, v. 49, no. 6, p. 657–661, doi:10.1130/G48333.1.

Cilliers, C. D., R. T. Tucker, J. L. Crowley, and L. E. Zanno, 2021, Age constraint for the Moreno Hill Formation (Zuni Basin) by CA-TIMS and LA-ICP-MS detrital zircon geochronology: PeerJ, v. 9, doi:10.7717/peerj.10948.

Collins, W. J., 1991, A reassessment of the 'Hunter-Bowen Orogeny': Tectonic implications for the southern New England Fold Belt: Australian Journal of Earth Sciences, v. 38, no. 4, p. 409–423, doi:10.1080/08120099108727981.

Corso, J. D. et al., 2020, Extinction and dawn of the modern world in the Carnian (Late Triassic): Science Advances, v. 6, no. 38, p. eaba0099, doi:10.1126/SCIADV.ABA0099.

Coutts, D. S., W. A. Matthews, and S. M. Hubbard, 2019, Assessment of widely used methods to derive depositional ages from detrital zircon populations: Geoscience Frontiers, v. 10, no. 4, p. 1421–1435, doi:10.1016/j.gsf.2018.11.002.

Damiani, R. J., and A. Warren, 1997, Re-interpretation of parotosuchus wadei cosgriff, a capitosaurid from the triassic narrabeen group at gosford, new south wales, with comments on its growth stage: Alcheringa, v. 21, no. 4, p. 281–289, doi:10.1080/03115519708619168.

Decelles, P. G., 2012, Foreland Basin Systems Revisited: Variations in Response to Tectonic Settings: Tectonics of Sedimentary Basins: Recent Advances, p. 405–426, doi:10.1002/9781444347166.CH20;CTYPE:STRING:BOOK.

Dickinson, W. R., and G. E. Gehrels, 2009, Use of U–Pb ages of detrital zircons to infer maximum depositional ages of strata: A test against a Colorado Plateau Mesozoic database: Earth and Planetary Science Letters, v. 288, no. 1–2, p. 115–125, doi:10.1016/J.EPSL.2009.09.013.

Dobbs, S. C., M. A. Malkowski, T. M. Schwartz, Z. T. Sickmann, and S. A. Graham, 2022, Depositional Controls on Detrital Zircon Provenance: An Example From Upper Cretaceous Strata, Southern Patagonia: Frontiers in Earth Science, v. 10, doi:10.3389/feart.2022.824930.

Exon, N. F. ., 1976, Geology of the Surat Basin in Queensland: Australian Government Pub. Service.

Fielding, C. R., and T. D. Frank, 2014, Abstract A Paleo-Polar to Mid-Latitudinal Transect Preserved in the Permian Succession of Eastern Australia: Trends in Facies, Stratal Stacking Patterns and Petroleum System Elements Through a Prolonged Icehouse Interval.

Fielding, C. R., T. D. Frank, K. Savatic, C. Mays, S. McLoughlin, V. Vajda, and R. S. Nicoll, 2022, Environmental change in the late Permian of Queensland, NE Australia: The warmup to the end-Permian Extinction: Palaeogeography, Palaeoclimatology, Palaeoecology, v. 594, doi:10.1016/j.palaeo.2022.110936.

Fielding, Christopher R, Rod J Holcombe, C R Fielding, C. 1 Stephens, and R J Holcombe, 1997, Permian stratigraphy and palaeogeography of the eastern Bowen Basin Permian stratigraphy and palaeogeography of the eastern Bowen Basin, Gogango Overfolded Zone and Strathmuir Synclinorium in the Rockhampton-Mackay region, central Queensland.

Fielding, C. R., and J. Kassan, 1996, Evolving depositional environments in the Triassic of the South-West End-Permian terrestrial mass extinction of Gondwana View project Cape Roberts Project View project.

Fielding, C. R., R. Sliwa, R. J. Holcombe, and J. Kassan, 1996, A NEW PALAEOGEOGRAPHIC SYNTHESIS OF THE BOWEN BASIN OF CENTRAL QUEENSLAND: Kassan & Fielding.

Finzel, E. S., S. N. Thomson, D. M. Pearson, L. K. Horkley, K. Garber, and C. Gardner, 2025, First cycle or polycyclic? Combining apatite and zircon detrital U-Pb geochronology and geochemistry to assess sediment recycling and effects of weathering: Earth and Planetary Science Letters, v. 650, doi:10.1016/j.epsl.2024.119131.

Fitch, A. J., M. Haas, W. C'Hair, E. Ridgley, B. Ridgley, D. Oldman, C. Reynolds, and D. M. Lovelace, 2023, A New Rhynchosaur Taxon from the Popo Agie Formation, WY: Implications for a Northern Pangean Early-Late Triassic (Carnian) Fauna: Diversity, v. 15, no. 4, p. 544, doi:10.3390/d15040544.

Foffa, D., S. J. Nesbitt, R. J. Butler, S. L. Brusatte, S. Walsh, N. C. Fraser, and P. M. Barrett, 2024, The osteology of the Late Triassic reptile Scleromochlus: The Anatomical Record, v. 307, no. 4, p. 1113–1146, doi:10.1002/ar.25335.

Foley, E. K., M. Baty, E. M. Knutsen, J. S. Lignum, and E. M. Roberts, 2020, Jurassic - Early Cretaceous paleogeography and paleoenvironments of the north-eastern margin of Gondwana: Insights from the Carpentaria Basin, Australia: Gondwana Research, v. 88, p. 126–149, doi:10.1016/j.gr.2020.07.003.

Foley, E. K., R. A. Henderson, E. M. Roberts, A. I. S. Kemp, C. N. Todd, E. M. Knutsen, C. Fisher, C. C. Wainman, and C. Spandler, 2021, Jurassic Arc: Reconstructing the Lost World of eastern Gondwana: Geology, v. 49, no. 11, p. 1391–1396, doi:10.1130/G49328.1.

Foley, E. K., E. M. Roberts, and E. M. Knutsen, 2022, Deciphering Late Cretaceous palaeo-river catchments in eastern Australia: Recognition of distinct northern and southern drainage basins: Basin Research, v. 34, no. 2, p. 590–617, doi:10.1111/bre.12632.

Golding, S. D., I. T. Uysal, M. Glikson, and F. Audsley, 2000, Thermal and fluid flow history in the Bowen Basin Miryam Glikson The thermal history of the Bowen Basin, Queensland, Australia: vitrinite reflectance and clay mineralogy of Late Permian coal measures.

Grech, P. V, 2001, Sedimentology and sequence stratigraphy of the Early Triassic Rewan Group, Bowen Basin, Doctoral dissertation: The University of Adelaide.

Green, P. M., D. C. Carmichael, T. J. Brain, C. G. Murray, J. McKellar, J. W. Beeston, and A. R. G. Gray, 1997, Lithostratigraphic units in the Bowen and Surat Basins, Queensland: The Surat and Bowen Basins, south-east Queensland, p. 41–108.

Guo, W., L. Tian, D. Chu, W. Shu, M. J. Benton, J. Liu, and J. Tong, 2025, Rapid riparian ecosystem recovery in low-latitudinal North China following the end-Permian mass extinction: doi:10.7554/eLife.104205.1.

Hamley, T., J. C. Cisneros, and R. Damiani, 2021, A procolophonid reptile from the Lower Triassic of Australia: 554–609 p.

Hancox, P. J., J. Neveling, and B. S. Rubidge, 2020, Biostratigraphy of the cynognathus assemblage zone (Beaufort group, Karoo supergroup), South Africa: South African Journal of Geology, v. 123, no. 2, p. 217–238, doi:10.25131/sajg.123.0016.

Henderson, R., C. Spandler, E. K. Foley, A. I. S. Kemp, E. M. Roberts, and C. Fisher, 2022, Early cretaceous tectonic setting of eastern Australia: Evidence from the subduction-related Morton Igneous Association of Southeast Queensland: Lithos, v. 410–411, doi:10.1016/j.lithos.2021.106573.

Herriott, T. M., J. L. Crowley, M. D. Schmitz, M. A. Wartes, and R. J. Gillis, 2019, Exploring the law of detrital zircon: LA-ICP-MS and CA-TIMS geochronology of Jurassic forearc strata, Cook Inlet, Alaska, USA: Geology, v. 47, no. 11, p. 1044–1048, doi:10.1130/G46312.1.

Hoy, D., 2020, The Hunter-Bowen Orogeny in eastern Australia.

Jenkins, R. B., B. Landenberger, and W. J. Collins, 2002, Late Palaeozoic retreating and advancing subduction boundary in the New England Fold Belt, New South Wales: Australian Journal of Earth Sciences, v. 49, no. 3, p. 467–489, doi:10.1046/j.1440-0952.2002.00932.x.

Jensen, A. R., 1975, Permo-Triassic stratigraphy and sedimentation in the Bowen Basin, Queensland: Canberra, viii–187 p.

Jessop, K., N. R. Daczko, and S. Piazolo, 2019, Tectonic cycles of the New England Orogen, eastern Australia: A Review: Taylor and Francis Ltd., p. 459–496, doi:10.1080/08120099.2018.1548378.

Kassan, J., 1994, Basin analysis of the Triassic succession, Bowen Basin, Queensland: The University of Queensland, doi:10.14264/293525.

Kear, B. P., and R. J. Hamilton-Bruce, 2019, Dinosaurs in Australia: Dinosaurs in Australia, doi:10.1071/9780643101692.

Korsch, R. J., G. Australia, D. L. Huston, R. A. Henderson, R. S. Blewett, and I. W. Withnall, n.d., Crustal architecture and geodynamics of North Queensland, Australia: Crustal architecture and geodynamics of North Queensland, Australia: insights from deep seismic reflection profiling insights from deep seismic reflection profiling.

Korsch, R. J., J. M. Totterdell, D. L. Cathro, and M. G. Nicoll, 2009, Early Permian East Australian Rift System: Australian Journal of Earth Sciences, v. 56, no. 3, p. 381–400, doi:10.1080/08120090802698703.

Korsch, R. J., J. M. Totterdell, T. Fomin, and M. G. Nicoll, 2009, Contractional structures and deformational events in the Bowen, Gunnedah and Surat Basins, eastern Australia: Australian Journal of Earth Sciences, v. 56, no. 3, p. 477–499, doi:10.1080/08120090802698745.

Lang, S. C., P. Grech, R. Root, A. Hill, and D. Harrison, 2001, THE APPLICATION OF SEQUENCE STRATIGRAPHY TO EXPLORATION AND RESERVOIR DEVELOPMENT IN THE COOPER-EROMANGA-BOWEN-SURAT BASIN SYSTEM: The APPEA Journal, v. 41, no. 1, p. 223, doi:10.1071/aj00011.

Ludwig K.R., 2009, User's Manual for Isoplot 3.70. A Geochronological Toolkit for Microsoft Excel: Berkley, Berkley Geochronology Centre Special Publication No.4.

Martínez, R. N., C. Apaldetti, O. A. Alcober, C. E. Colombi, P. C. Sereno, E. Fernandez, P. S. Malnis, G. A. Correa, and D. Abelin, 2012, Vertebrate succession in the Ischigualasto Formation: Journal of Vertebrate Paleontology, v. 32, no. sup1, p. 10–30, doi:10.1080/02724634.2013.818546.

Mays, C., and S. McLoughlin, 2022, END-PERMIAN BURNOUT: THE ROLE OF PERMIAN–TRIASSIC WILDFIRES IN EXTINCTION, CARBON CYCLING, AND ENVIRONMENTAL CHANGE IN EASTERN GONDWANA: Palaios, v. 37, no. 6, p. 292–317, doi:10.2110/palo.2021.051.

McElwain, J. C., and S. W. Punyasena, 2007, Mass extinction events and the plant fossil record: p. 548–557, doi:10.1016/j.tree.2007.09.003.

McKellar, J. L. et al., 2015, CA-IDTIMS dating of tuffs, calibration of palynostratigraphy and stratigraphy of the Bowen and Galilee basins.

McLoughlin, S., C. Mays, V. Vajda, M. Bocking, T. D. Frank, and C. R. Fielding, 2020, Dwelling in the dead zone-vertebrate burrows immediately succeeding the end-permian extinction event in Australia: Palaios, v. 35, no. 8, p. 342–357, doi:10.2110/PALO.2020.007.

Metcalfe, I., S. Denyszyn, R. Mundil, J. Esterle, and G. R. Shi, 2024, High-precision CA-IDTIMS U-Pb chronostratigraphy in the Bowen Basin, eastern Australia, calibration of deep-time climate change, super-volcanism and mass extinction: Gondwana Research, v. 133, p. 335–347, doi:10.1016/j.gr.2024.07.001.

Michaelsen, P., 2002, Mass extinction of peat-forming plants and the effect on fluvial styles across the Permian-Triassic boundary, northern Bowen Basin, Australia: Palaeogeography, Palaeoclimatology, Palaeoecology, v. 179, no. 3–4, p. 173–188, doi:10.1016/S0031-0182(01)00413-8.

Michaelsen, P., and R. A. Henderson, 2000, Sandstone petrofacies expressions of multiphase basinal tectonics and arc magmatism: Permian-Triassic north Bowen Basin, Australia: Sedimentary Geology, v. 136, no. 1–2, p. 113–136, doi:10.1016/S0037-0738(00)00090-7.

Milan, L. A., E. A. Belousova, R. A. Glen, T. Chapman, J. Kalmbach, B. Fu, and P. M. Ashley, 2021, A New Reconstruction for Permian East Gondwana Based on Zircon Data From Ophiolite of the East Australian Great Serpentinite Belt: Geophysical Research Letters, v. 48, no. 1, doi:10.1029/2020GL090293.

Mundil, R., K. R. Ludwig, I. Metcalfe, and P. R. Renne, 2004, Age and Timing of the Permian Mass Extinctions: U/Pb Dating of Closed-System Zircons.

Naher, J., C. R. Fielding, and M. A. Martin, 2025, Misleading Basin Margins—Analysis of the Upper Permian Succession in the Retroarc Foreland Bowen Basin of Northeast Australia: Basin Research, v. 37, no. 3, p. e70033, doi:10.1111/BRE.70033;REQUESTEDJOURNAL:JOURNAL:13652117;WGROUP:STRING:PUBLICATION.

Nicoll, R. S., J. R. Laurie, S. Bodorkos, J. Crowley, and T. E. Smith, 2015, The Impact of CA-IDTIMS on the Understanding of Permian and Triassic Lithostratigraphy and Correlation in Eastern Australian Coal Basins: Society of Exploration Geophysicists, p. 41–41, doi:10.1190/ice2015-2210728.

Nield, C. M., R. Damiani, and A. Warren, 2006, A short-snouted trematosauroid (Tetrapoda Temnospondyli) from the Early Triassic of Australia: The oldest known trematosaurine: Alcheringa, v. 30, no. 2, p. 263–271, doi:10.1080/03115510608619317;JOURNAL:JOURNAL:TALC20;REQUESTEDJOURNAL:JOURNAL:TALC20;WGROUP:STRING:PUBLICATION.

Northwood, C., 1999, Actinopterygians from the early Triassic Arcadia Formation, Queensland, Australia: Memoirs of the Queensland Museum, v. 43, p. 787–796.

Northwood, C., 2005, Early Triassic coprolites from Australia and their palaeobiological significance: Palaeontology, v. 48, no. 1, p. 49–68, doi:10.1111/J.1475-4983.2004.00432.X.

Othman, and Rushdy, 2003, Petroleum geology of the Gunnedah-Bowen-Surat Basins, Northern New South Wales : stratigraphy, organic petrology and organic geochemistry: doi:10.26190/unsworks/21635.

Paton, C., J. Hellstrom, B. Paul, J. Woodhead, and J. Hergt, 2011, Iolite: Freeware for the visualisation and processing of mass spectrometric data: Journal of Analytical Atomic Spectrometry, v. 26, no. 12, p. 2508–2518, doi:10.1039/C1JA10172B.

Phillips, L. J., S. A. Edwards, V. Bianchi, and J. S. Esterle, 2017, Paleo-environmental reconstruction of Lopingian (upper Permian) sediments in the Galilee Basin, Queensland, Australia: Australian Journal of Earth Sciences, v. 64, no. 5, p. 587–609, doi:10.1080/08120099.2017.1338618.

Phillips, L. J., C. Verdel, C. M. Allen, and J. S. Esterle, 2018, Detrital zircon U–Pb geochronology of Permian strata in the Galilee Basin, Queensland, Australia: Australian Journal of Earth Sciences, v. 65, no. 4, p. 465–481, doi:10.1080/08120099.2018.1467261.

Retallack, G. J., 2021, Multiple Permian-Triassic life crises on land and at sea: Global and Planetary Change, v. 198, p. 103415, doi:10.1016/J.GLOPLACHA.2020.103415.

Retallack, G. J., A. H. Jahren, N. D. Sheldon, R. Chakrabarti, C. A. Metzger, and R. M. H. Smith, 2005, The Permian-Triassic boundary in Antarctica: Antarctic Science, v. 17, no. 2, p. 241–258, doi:10.1017/S0954102005002658.

Roberts, A. J., M. Rucinski, B. P. Kear, Ø. Hammer, V. S. Engelschiøn, T. H. Scharling, R. B. Larsen, and J. H. Hurum, 2025, Earliest oceanic tetrapod ecosystem reveals rapid complexification of Triassic marine communities: Science, v. 390, no. 6774, p. 722–727, doi:10.1126/science.adx7390.

Romano, M., M. Bernardi, F. M. Petti, B. Rubidge, J. Hancox, and M. J. Benton, 2020, Early Triassic terrestrial tetrapod fauna: a review: Elsevier B.V., doi:10.1016/j.earscirev.2020.103331.

Rosenbaum, G., A. Slade, and D. Hoy, 2020, Sedimentological responses to the Hunter–Bowen Orogeny (eastern Australia): evidence from the northern Gympie Terrane: Australian Journal of Earth Sciences, v. 67, no. 1, p. 59–73, doi:10.1080/08120099.2019.1648317.

Rozefelds, A. C., A. Warren, A. Whitfield, and S. Bull, 2011, New evidence of large Permo-Triassic dicynodonts (Synapsida) from Australia: Journal of Vertebrate Paleontology, v. 31, no. 5, p. 1158–1162, doi:10.1080/02724634.2011.595858.

Sliwa, R., A. Babaahmadi, and J. Esterle, 2018, ACARP Project C24032: Structure Supermodel 2017-Fault Characterisation in Permian to Jurassic Coal Measures For the Australian Coal Association Research Program (ACARP).

Smith, T. E. et al., 2017, The Impact of Recalibrating Palynological Zones to the Chronometric Timescale: Revised Stratigraphic Relationships in Australian Permian and Triassic Hydrocarbon-Bearing Basins*.

Smith, T., R. Nicoll, J. Laurie, J. Crowley, J. McKellar, H. Campbell, I. Raine, D. Mantle, and A. Mory, 2018, Recalibrating Australian Triassic Palynostratigraphy to the International Geologic Timescale Using High Resolution CA-IDTIMS Dating: ASEG Extended Abstracts, v. 2018, no. 1, p. 1–1, doi:10.1071/ASEG2018ABP010.

Sobczak, K. et al., 2024, Palynostratigraphy and Bayesian age stratigraphic model of new CA-ID-TIMS zircon ages from the Walloon Coal Measures, Surat Basin, Australia: Gondwana Research, v. 132, p. 150–167, doi:10.1016/J.GR.2024.04.012.

Sun, Y., M. M. Joachimski, P. B. Wignall, C. Yan, Y. Chen, H. Jiang, L. Wang, and X. Lai, 2012, Lethally Hot Temperatures During the Early Triassic Greenhouse: Source: Science, New Series, v. 338, no. 6105, p. 366–370, doi:10.1126/science.l226528.

Todd, C. N., E. M. Roberts, and A. J. Charles, 2022, A revised Permian–Triassic stratigraphic framework for the northeastern Galilee Basin, Queensland, Australia, and definition of a new Middle–Upper Triassic sedimentary unit: Australian Journal of Earth Sciences, v. 69, no. 1, p. 113–134, doi:10.1080/08120099.2021.1931962.

Todd, C. N., E. M. Roberts, E. M. Knutsen, A. C. Rozefelds, H. Q. Huang, and C. Spandler, 2019, Refined age and geological context of two of Australia's most important Jurassic vertebrate taxa (Rhoetosaurus brownei and Siderops kehli), Queensland: Gondwana Research, v. 76, p. 19–25, doi:10.1016/j.gr.2019.05.008.

Tucker, R. T., E. M. Roberts, V. Darlington, and S. W. Salisbury, 2017, Investigating the stratigraphy and palaeoenvironments for a suite of newly discovered mid-Cretaceous vertebrate fossil-localities in the Winton Formation, Queensland, Australia: Sedimentary Geology, v. 358, p. 210–229, doi:10.1016/j.sedgeo.2017.05.004.

Tucker, R. T., E. M. Roberts, R. A. Henderson, and A. I. S. Kemp, 2016, Large igneous province or long-lived magmatic arc along the eastern margin of Australia during the Cretaceous? Insights from the sedimentary record: Bulletin of the Geological Society of America, v. 128, no. 9–10, p. 1461–1480, doi:10.1130/B31337.1.

Tucker, R. T., E. M. Roberts, Y. Hu, A. I. S. Kemp, and S. W. Salisbury, 2013, Detrital zircon age constraints for the Winton Formation, Queensland: Contextualizing Australia's Late Cretaceous dinosaur faunas: Gondwana Research, v. 24, no. 2, p. 767–779, doi:10.1016/J.GR.2012.12.009.

Uysal, I. T., M. Glikson, S. D. Golding, and F. Audsley, 2000, The thermal history of the Bowen Basin, Queensland, Australia: vitrinite reflectance and clay mineralogy of Late Permian coal measures: Tectonophysics, v. 323, no. 1–2, p. 105–129, doi:10.1016/S0040-1951(00)00098-6.

Vermeesch, P., 2018, IsoplotR: A free and open toolbox for geochronology: Geoscience Frontiers, v. 9, no. 5, p. 1479–1493, doi:10.1016/J.GSF.2018.04.001.

Vermeesch, P., 2021, Maximum depositional age estimation revisited: Geoscience Frontiers, v. 12, no. 2, p. 843–850, doi:10.1016/J.GSF.2020.08.008.

Warren, A., 1981, A horned member of the labyrinthodont superfamily brachyopoidea from the early triassic of Queensland: Alcheringa, v. 5, no. 4, p. 273–288, doi:10.1080/03115518108566995.

Warren, A. A., 1980, Parotosuchus from the early triassic of Queensland and Western australia: Alcheringa, v. 4, no. 1, p. 25–36, doi:10.1080/03115518008558978.

Warren, A. A., 1985, Two long-snouted temnospondyls (Amphibia, labyrinthodontia) from the triassic of queensland: Alcheringa, v. 9, no. 4, p. 293–295, doi:10.1080/03115518508618974.

Warren, A., and T. Black, 1985, A New Rhytidosteid (Amphibia, Labyrinthodontia) from the Early Triassic Arcadia Formation of Queensland, Australia, and the Relationships of Triassic Temnospondyls: Journal of Vertebrate Paleontology, v. 5, no. 4, p. 303–327.

Warren, A., R. J. Damiani, and A. M. Yates, 2001, Palaeobiogeography of Australian fossil amphibians: Historical Biology, v. 15, no. 1–2, p. 171–179, doi:10.1080/10292380109380589.

Warren, A. A., R. Damiani, and A. M. Yates, 2006, The South African stereospondyl Lydekkerina huxleyi (Tetrapoda, Temnospondyli) from the Lower Triassic of Australia: Geological Magazine, v. 143, no. 6, p. 877–886, doi:10.1017/S0016756806002524.

Warren, A. A., and M. N. Hutchinson, 1987, The skeleton of a new hornless rhytidosteid (Amphibia, temnospondyli): Alcheringa, v. 11, no. 4, p. 291–302, doi:10.1080/03115518708619138.

Warren, A., and C. Marsicano, 2000, A Phylogeny of the Brachyopoidea (Temnospondyli, Stereospondyli): Journal of Vertebrate Paleontology, v. 20, no. 3, p. 462–483.

Warren, A., and C. Marsicano, 1998, Revision of the brachyopidae (temnospondyli) from the triassic of the sydney, carnarvon and tasmania basins, Australia: Alcheringa, v. 22, no. 4, p. 329–342, doi:10.1080/03115519808619331.

Warren, A., A. C. Rozefelds, and S. Bull, 2011, Tupilakosaur-like vertebrae in Bothriceps australis, an Australian brachyopid stereospondyl: Journal of Vertebrate Paleontology, v. 31, no. 4, p. 738–753, doi:10.1080/02724634.2011.590563.

Zhao, Xiangdong et al., 2025, Climate–carbon-cycle interactions and spatial heterogeneity of the late Triassic Carnian pluvial episode: Nature Communications, v. 16, no. 1, p. 5404, doi:10.1038/s41467-025-61262-7.

Appendix

4.1 Bandanna Formation & Rangal Coal Measures (Permian tuffs)

Outcrops — none analysed.

Cores – Rewan-1, 563.1 m (Bandanna Formation tuffaceous mudstone). Zircons grain morphology contains a mixed population dominated by short prismatic to equant subhedral grains with fine oscillatory to patchy zoning and sporadic thin bright rims; several grains appear slightly rounded. Long axes are about 70–160 µm. 100 zircon grains analysed; 38 concordant (5% discordance). Weighted mean = 250.0 ± 1.2 Ma (n = 38, MSWD = 1.13); Concordia = 251.4 ± 1.2 Ma (n = 38, MSWD = 0.40). These ages correspond to the latest Changhsingian to earliest Induan, i.e., the Permian–Triassic boundary interval.

Drake NS27, 275.6 m (Rangal Coal Measures tuff). Zircons are chiefly euhedral prismatic with pronounced oscillatory zoning and sharp terminations; inherited cores and subtle resorption embayment’s are present in a subset. Long axes are about 90–240 µm. 64 grains analysed; 22 concordant (5%). Weighted mean = 251.7 ± 1.7 Ma (n = 22, MSWD = 1.5); Concordia = 252.6 ± 1.2 Ma (n = 22, MSWD = 1.5). This corresponds to the Changhsingian (latest Permian).

Theodore NS150, 171.5 m (Rangal Coal Measures tuffaceous debris-flow). Zircons grain morphology are mostly euhedral to subhedral and elongate prismatic with clear oscillatory zoning and occasional bright CL rims; a few grains show rounded margins or resorption features. Long axes are typically about 90–220 µm. 167 grains analysed; 72 concordant (5%). Weighted mean = 250.5 ± 0.95 Ma (n = 72, MSWD = 1.7); Concordia = 251.8 ± 0.6 Ma (n = 72, MSWD = 1.7). These ages correspond to the latest Changhsingian–earliest Induan, i.e., the P–T boundary interval.

4.2 Sagittarius Sandstone (Lower Rewan)

Outcrops — Early Storms Creek (outcrop). 300 analyses; 121 concordant (40%). YSG 233.9 ± 4.7 Ma; YDZ 234.3 (+4.6/−5.7) Ma; YGC2σ 246.4 ± 2.5 Ma (n = 5, MSWD = 1.01); YSP 246.4 ± 3.8 Ma (n = 5, MSWD = 1.01); MLA 237.6 ± 4.7 Ma. An MLA of ca. 238 Ma corresponds to the late Anisian–early Ladinian (Middle Triassic).

Cores — Rewan-1, 473.5 m (lower part). 300 analyses; 202 concordant (67%). YSG 230.2 ± 4.8 Ma; YDZ 227.7 (+2.7/−4.4) Ma; YGC2σ 234.4 ± 1.2 Ma (n = 27, MSWD = 1.30); YSP 233.8 ± 2.8 Ma (n = 22, MSWD = 1.00); MLA 233.2 ± 2.2 Ma. An MLA of ca. 233 Ma corresponds to the early Carnian (Late Triassic).

Rewan-1, 412.1 m (upper part). 302 analyses; 262 concordant (87%). YSG 230.8 ± 7.3 Ma; YDZ 229.7 (+3.7/−5.7) Ma; YGC2σ 236.7 ± 1.3 Ma (n = 14, MSWD = 1.14); YSP 236.4 ± 2.9 Ma (n = 13, MSWD = 1.03); MLA 237.7 ± 2.5 Ma. An MLA of ca. 237 Ma corresponds to the latest Ladinian–earliest Carnian.

Drake NS27, 131.9 m. 300 analyses; 200 concordant (67%). YSG 242.5 ± 5.8 Ma; YDZ 240.3 (+2.8/−5.3) Ma; YGC2σ 246.0 ± 2.0 Ma (n = 20, MSWD = 1.07); YSP 246.0 ± 2.8 Ma (n = 21, MSWD = 0.64); MLA 245.9 ± 1.9 Ma. An MLA of ca. 246 Ma corresponds to the late Anisian (Middle Triassic).

Brumby Plains-1, 183.3 m. 300 analyses; 176 concordant (59%). YSG 241.11 ± 6.00 Ma; YDZ 238.33 (+4.4/−5.7) Ma; YGC2σ 247.7 ± 1.6 Ma (n = 21, MSWD = 0.90); YSP 248.0 ± 3.0 Ma (n = 22, MSWD = 0.98); MLA 249.8 ± 2.7 Ma. An MLA of ca. 250 Ma corresponds to the Olenekian (Early Triassic).

4.3 Arcadia Formation (Upper Rewan)

Outcrops — The Crater. 363 analyses; 142 concordant (39%). YSG 231.5 ± 5.6 Ma; YDZ 229.0 (+3.7/−5.8) Ma; YGC2σ 236.9 ± 1.2 Ma (n = 22, MSWD = 0.76); YSP 238.0 ± 2.9 Ma (n = 29, MSWD = 0.99); MLA 239.0 ± 1.6 Ma. An MLA of ca. 239 Ma corresponds to the late Ladinian (Middle Triassic).

Oaky Creek. 334 analyses; 195 concordant (58%). YSG 229.3 ± 10.3 Ma; YDZ 227.9 (+5.3/−10.0) Ma; YGC2σ 236.2 ± 2.1 Ma (n = 13, MSWD = 0.82); YSP 238.3 ± 2.9 Ma (n = 21, MSWD = 0.99); MLA 239.2 ± 3.1 Ma. An MLA of ca. 239 Ma corresponds to the late Ladinian (Middle Triassic).

Duckworth Creek. 301 analyses; 187 concordant (62%). YSG 228.5 ± 6.2 Ma; YDZ 225.7 (+3.0/−5.5) Ma; YGC2σ 233.2 ± 1.3 Ma (n = 24, MSWD = 0.77); YSP 235.9 ± 2.1 Ma (n = 31, MSWD = 0.98); MLA 235.9 ± 2.0 Ma. An MLA of ca. 236 Ma corresponds to the early Carnian (Late Triassic).

Detrital apatite U–Pb (Duckworth Creek). Forty-nine apatite analyses from the same sandstone yield a Tera–Wasserburg lower intercept age of **239.3 ± 6.6 Ma** (2σ; MSWD = 0.79; n = 49; ^204Pb based common Pb correction; Fig. 8). This intercept corresponds to the late Carnian (Late Triassic). Within uncertainty, the apatite minimum age is consistent with the zircon-based depositional constraints for this horizon (MLA = 235.9 ± 2.1 Ma; YGC2σ = 233.2 ± 1.3 Ma; YSP = 235.9 ± 2.1 Ma), supporting a Carnian MDA for the Duckworth Creek bed.

Cores — Taroom 14, 1144.4 m. 300 analyses; 279 concordant (93%). YSG 230.5 ± 2.3 Ma; YDZ 228.3 (+3.1/−5.7) Ma; YGC2σ 236.4 ± 2.4 Ma (n = 18, MSWD = 0.64); YSP 237.8 ± 1.6 Ma (n = 40, MSWD = 0.98); MLA 237.8 ± 1.6 Ma. An MLA of ca. 237 Ma corresponds to the late Ladinian–early Carnian.

4.4 Clematis Group

Outcrops — Mount Round (basal Clematis). 320 analyses; 186 concordant (58%). YSG 223.8 ± 6.9 Ma; YDZ 222.1 (+5.6/−6.2) Ma; YGC2σ 229.3 ± 3.8 Ma (n = 7, MSWD = 1.70); YSP 227.5 ± 3.9 Ma (n = 5, MSWD = 1.15); MLA 227.4 ± 6.1 Ma. An MLA of ca. 227 Ma corresponds to the late Carnian (Late Triassic).

Cores — none analysed.